Tuning effective dynamical properties of periodic media by FFT-accelerated topological optimization

Rémi Cornaggia, Cédric Bellis

Received: Added at production | Revised: Added at production | Accepted: Added at production

DOI: xxx/xxxx

RESEARCH ARTICLE

Tuning effective dynamical properties of periodic media by FFT-accelerated topological optimization

R. Cornaggia* | C. Bellis

[1]Aix-Marseille Univ, CNRS, Centrale Marseille, LMA UMR 7031, Marseille, France

Correspondence
*Rémi Cornaggia,
LMA, 4 impasse Nikola Tesla,
CS 40006, 13453 Marseille Cedex 13,
France.
Email: cornaggia@lma.cnrs-mrs.fr

Abstract

This works concerns the propagation of waves in periodic media, whose microstructure is optimized to obtain specific dynamical properties (typically, to maximize the dispersion in given directions). The present study, focusing on scalar waves in two dimensions, *e.g.* antiplane shear waves, aims at setting a generic optimization framework. The proposed optimization procedure relies on a number of mathematical and numerical tools. First, the two-scale asymptotic homogenization method is deployed up to second-order to provide an effective dispersive model. Simple dispersion indicators and cost functionals are then considered on the basis of this model. Then, the minimization of these functionals is performed thanks to an algorithm that relies on the concept of topological derivative to iteratively perform phase changes in the unit cell characterizing the material. Finally, FFT-accelerated solvers are extensively used to solve the cell problems underlying the homogenized model. To illustrate the proposed approach, the resulting procedure is applied to the design of anisotropic media with maximal dispersion in specific directions, and to the reconstruction of unknown microstructures from effective phase velocity data.

KEYWORDS:
Phononic crystals; Dispersive waves; Second-order homogenization; Topological derivatives

1 | INTRODUCTION

The interest for *sonic* and *phononic crystals*[1], *i.e.* (most often) periodically microstructured composites supporting acoustic or elastic wave propagation, has been growing in the past years. These structures, also often called *metameterials*[2,3], present exceptional dispersive properties. In particular, for specific range of frequencies (the so-called *band-gaps*), only exponentially decaying waves can propagate through the structure, due to inner resonances[4,5,6] or Bragg effects. These properties make them ideal candidates for a wide range of applications[3], from sound insulators[7] to directional wave propagation[8] and seismic protections[5].

To determine good candidates of microstructure that exhibit these phenomena or to tune their characteristics, many optimization strategies were developed. For metamaterials realized from selected geometric designs, *e.g.* laminated composites or arrays of specific resonators[4,5], one aims at optimizing the physical or geometric parameters of these designs. For situations where only the constitutive materials of the sought composite are imposed, *topological* optimization procedures, determining the distribution of these materials, are deployed.

Many of these optimization strategies (see *e.g.* the works[4,9,8]) lean on the Floquet-Bloch theory that describes standing waves in periodic composites[10,1]. This approach covers all frequencies but requires the (possibly costly) computation of eigenfrequencies and eigenmodes of the Bloch problems. If one is interested only in a specific band of frequencies (*e.g.* the low-frequency

regime, or near one of the Bloch frequency), an alternative way is to rely instead on an *effective* description of the material, given by an homogenization process [10,11], and the cost functional to be minimized can be written in terms of the coefficients of the considered effective model. In particular, the *two-scale asymptotic homogenization* [10] is a convenient choice, as the effective coefficients are determined from the solutions of *cell problems* posed on the periodicity cell. Standard PDE-constraint optimization algorithms can then be used on the basis of these cell problems. This approach is commonly used in static to optimize the stiffness properties of elastic composites *e.g.* [12,13,14]. It was recently extended to the optimization of the low-frequency dynamics of regular [15] and highly-contrasted composites [6], and also to higher-frequency regimes [16] (in this latter case, both Bloch eigenvalue problems and asymptotic homogenization are needed to describe the wave motion [17,18]).

In the present paper, as in [15], we focus on the low-frequency dispersive effects of periodic materials, using the effective description provided by the *second-order* asymptotic homogenization [19,20] to set the optimization problem. The effective wave equation is then enriched with additional micro-stiffness and micro-inertia terms featuring higher-order derivatives of the wavefield, similarly to the so-called *gradient elasticity* models [21,22]. The dispersive effects are described by the tensor-valued coefficients that characterize these additional terms (*e.g.* the so-called fourth-order *Burnett tensor* [20]). The microstructures corresponding to the bounds of these tensors (*i.e.* to minimal or maximal amplitudes of dispersive effects) are known analytically only in simplified 1D cases [23] or for specific classes of microstructures [24]. Efficient topological optimization procedures are therefore needed to provide optimal microstructures in more general settings, and the present paper aims at providing a simple and efficient approach. It differs from [15] as (i) it permits non-constant density (ii) it uses an optimization algorithm [25,26] based on the *topological derivatives* of the effective coefficients [27] rather than their shape derivatives, and (iii) it takes advantage of a FFT-accelerated method to solve cell problems, instead of finite element methods.

Precising point (iii), the FFT-accelerated method was initially proposed by Moulinec and Suquet [28] to solve the first cell (or corrector) problem that appears in leading-order homogenization, in the context of linear and nonlinear elastostatics. Although well-known in the mechanical engineering litterature, the method was applied only recently to the additional cell problems stemming from higher-order homogenization [29,30]. At our knowledge, it was never used in a microstructure optimization procedure to enhance dynamic properties.

The article is organized as follows. In the Section 2, we precise the considered optimization problem and provide the necessary theoretical framework, including second-order homogenization of the wave equation and topological derivatives of effective coefficients. Section 3 is dedicated to the algorithmic features of the proposed method, namely the FFT-accelerated solver for cell problems and the material update steps in the optimization process. Section 4 presents two examples of applications: (i) optimization of two-phase composites to maximize the effective dispersion in given directions (including comparison with known analytical results for bilaminates), and (ii) identification of a periodic structure from phase velocity data gathered for several frequencies and propagation direction. In example (i), we also compute and discuss the first Floquet-Bloch eigenvalues of the obtained optimal unit cell. We finally summarize the results and discuss possible extensions in Section 5. Mathematical notations are gathered in Appendix.

2 | PROBLEM SETTING AND TOPOLOGICAL OPTIMIZATION

We consider a two-dimensional periodic composite material that is composed of cells $Y_\ell = \ell Y$, whose geometry is defined relatively to a *unit cell* Y owing to a reference lengthscale ℓ. Moreover, one assumes that the medium is characterized by a set of two Y-periodic fields $\boldsymbol{m} = (\rho, \mu)$ so that the constitutive property fields $\boldsymbol{x} \mapsto \rho(\boldsymbol{x}/\ell)$ and $\boldsymbol{x} \mapsto \mu(\boldsymbol{x}/\ell)$ are Y_ℓ-periodic. In other words, the material distribution of the microstructure are characterized by fluctuations at a scale associated with the variable $\boldsymbol{y} \overset{\text{def}}{=} \boldsymbol{x}/\ell$.

We consider time-hamonic waves in such a medium with dependency on the circular frequency ω. Accordingly, the amplitude u_ℓ of these waves obeys the equation:

$$\operatorname{div}\left(\mu\left(\frac{\boldsymbol{x}}{\ell}\right)\boldsymbol{\nabla} u_\ell(\boldsymbol{x})\right) + \rho\left(\frac{\boldsymbol{x}}{\ell}\right)\omega^2 u_\ell(\boldsymbol{x}) = 0. \tag{1}$$

Expressed in terms of a generic scalar field $u_\ell(\boldsymbol{x})$, the time-harmonic wave equation (1) is relevant to a number of physical configurations, such as acoustics where u_ℓ is the pressure field, or antiplane elasticity –retained hereafter as in previous works [19,27]– for which the latter stands for the out-of-plane displacement field, whereas ρ and μ are the density and shear modulus of the constitutive material(s) of the microstructure, respectively. Reference can be made to, *e.g.* ,[11,31] for other relevant models.

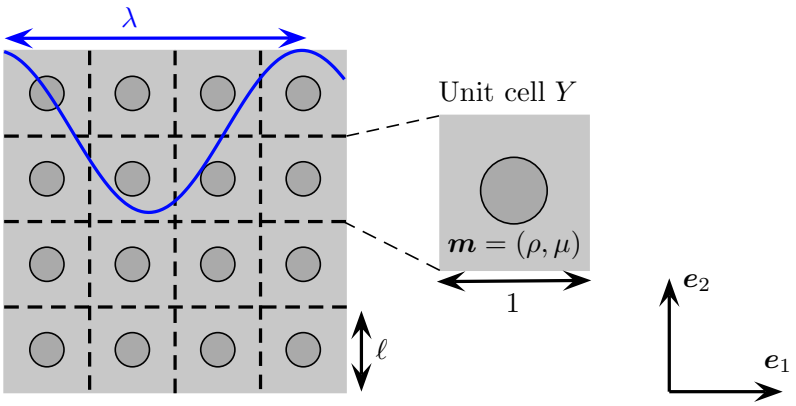

FIGURE 1 Time-harmonic wave in a 2D periodic medium with unit cell Y.

2.1 | Second-order homogenized model

The two-scales asymptotic homogenization procedure, introduced in the seventies[10,32], is applied to the field equation (1) to obtain an effective model with homogeneous coefficients. In this section, we recall the main results obtained through an asymptotic expansion of the solution at the second-order. We refer to[33,19,20,27] and the references therein for details and justifications of these results.

Two-scale asymptotic expansion

The asymptotic analysis relies on two main assumptions: (i) We place ourselves in the low-frequency and low-wavenumber regime, and therefore assume that there exists a *macroscopic wavelength* λ associated with u_ℓ (to be defined more precisely later on, see Remark 3), which is large enough for the scale separation assumption $\ell \ll \lambda$ to hold. (ii) Considering the small parameter $\varepsilon = \ell/\lambda$, we assume that the constitutive material properties μ and ρ do not depend on ε. Under these assumptions, (i) looking for a solution as a function of both the "slow" and "fast" variables $\boldsymbol{x}$ and $\boldsymbol{x}/\ell$, *i.e.* $u_\ell(\boldsymbol{x}) = u(\boldsymbol{x}, \boldsymbol{x}/\ell)$, (ii) expanding this unknown function u in terms of ε and (iii) performing an asymptotic analysis of the equation (1) when u_ℓ is replaced by this expansion results in the following formal expansion for u_ℓ:

$$u_\ell(\boldsymbol{x}) = U(\boldsymbol{x}) + \ell\, \boldsymbol{P}_1\Big(\frac{\boldsymbol{x}}{\ell}\Big) \cdot \boldsymbol{\nabla} U(\boldsymbol{x}) + \ell^2 \boldsymbol{P}_2\Big(\frac{\boldsymbol{x}}{\ell}\Big) : \boldsymbol{\nabla}^2 U(\boldsymbol{x}) + \ell^3 \boldsymbol{P}_3\Big(\frac{\boldsymbol{x}}{\ell}\Big) :\cdot \boldsymbol{\nabla}^3 U(\boldsymbol{x}) + o(\varepsilon^3), \tag{2}$$

with the notations of Appendix A.1. In Equation (2) U is a *macroscopic field* that depends only on the "slow" variable $\boldsymbol{x}$ and embeds the leading-order slow variations of u_ℓ, while $\boldsymbol{P}_j$ for $j \in \{1,2,3\}$ is a *cell function*, Y-periodic and mean-free, which depends on the "fast" variable $\boldsymbol{y}$ defined above and describes oscillations around U due to the microstructure. As seen, the amplitude of these perturbations depend linearly on the successive gradients of U: the cell functions, also called *localization tensors*[29], reflect the response of the microstructure to the slope $\boldsymbol{\nabla} U$, curvature $\boldsymbol{\nabla}^2 U$ and higher-order derivatives of the mean field.

Cell functions and effective properties

The cell functions $\boldsymbol{P}_j$ with $j \in \{1,2,3\}$ appear in the asymptotic procedure and in expansions such as (2) as factors of the successive gradients of mean fields (in the sense of the inner product between tensors). Therefore, $\boldsymbol{P}_j$ is defined as a *completely symmetric* tensor of order j, *i.e.* a tensor that is invariant by any permutation of its indices[19], so that it has $(j+1)$ independent components in $\mathbb{R}^2$. These functions are found to be the solutions of *static* periodic problems formulated in the reference unit cell Y, whose unit outward normal is denoted as $\boldsymbol{n}$, and for a generic tensor-valued cell function $\boldsymbol{P}$, by:

$$\begin{cases} \text{(i)} & \langle \boldsymbol{P} \rangle = \boldsymbol{0}, \qquad \boldsymbol{P} \text{ periodic on } \partial Y, \\ \text{(ii)} & \boldsymbol{S}(\boldsymbol{y}) = \mu(\boldsymbol{y}) \left[\boldsymbol{E}(\boldsymbol{y}) + \boldsymbol{\nabla} \boldsymbol{P}(\boldsymbol{y}) \right], \\ \text{(iii)} & \operatorname{div} \boldsymbol{S}(\boldsymbol{y}) + \boldsymbol{f}(\boldsymbol{y}) = \boldsymbol{0}, \end{cases} \tag{3}$$

where $\langle\cdot\rangle$ denotes the averaging operator over the unit cell Y, *i.e.*

$$\langle f\rangle = \frac{1}{|Y|}\int_Y f(\boldsymbol{y})\,\mathrm{d}\boldsymbol{y}.$$

and we introduced an auxiliary field $\boldsymbol{S}$, referred to as *cell stress* hereinafter, for short-hand notations. The loadings of the problem (3) are the prestrain $\boldsymbol{E}$ and the body force $\boldsymbol{f}$ that must be mean-free, *i.e.* $\langle\boldsymbol{f}\rangle = \boldsymbol{0}$, for the problem to be well-posed [10].

Cell function $\boldsymbol{P}$	Prestrain $\boldsymbol{E}$	Body force $\boldsymbol{f}$
$\boldsymbol{P}_1$	$\boldsymbol{E}_1 = \boldsymbol{I}$	$\boldsymbol{f}_1 = \boldsymbol{0}$
$\boldsymbol{P}_2$	$\boldsymbol{E}_2 = [\boldsymbol{I}\otimes\boldsymbol{P}_1]^{\mathrm{psym}}$	$\boldsymbol{f}_2 = \mu[\boldsymbol{I}+\boldsymbol{\nabla}\boldsymbol{P}_1]^{\mathrm{sym}} - (\rho/\varrho_0)\boldsymbol{\mu}_0$
$\boldsymbol{P}_3$	$\boldsymbol{E}_3 = [\boldsymbol{I}\otimes\boldsymbol{P}_2]^{\mathrm{psym}}$	$\boldsymbol{f}_3 = \mu[\boldsymbol{I}\otimes\boldsymbol{P}_1+\boldsymbol{\nabla}\boldsymbol{P}_2]^{\mathrm{sym}} - (\rho/\varrho_0)[\boldsymbol{\mu}_0\otimes\boldsymbol{P}_1]^{\mathrm{sym}}$

TABLE 1 Notations and values of the prestrain and body force for the direct cell problems.

For $j\in\{1,2,3\}$ the cell functions $\boldsymbol{P}_j$ are determined recursively as the solutions to (3) with the terms $\boldsymbol{E}$ and $\boldsymbol{f}$ being given in Table 1, where $\boldsymbol{I}$ is the second-order identity tensor while $\cdot^{\mathrm{psym}}$ and $\cdot^{\mathrm{sym}}$ denote respectively partial and complete tensor symmetrization, see Appendix A.1. Table 1 also features the constant parameters ϱ_0 and $\boldsymbol{\mu}_0$, which are effective properties corresponding to the *zero-th order homogenization*, respectively a scalar and a symmetric second-order tensor. These effective properties together with their high-order counterparts are defined as

$$\varrho_0 = \langle\rho\rangle, \qquad \boldsymbol{\varrho}_2 = \big\langle\rho\boldsymbol{P}_2\big\rangle, \qquad \boldsymbol{\mu}_0 = \Big\langle\mu\big[\boldsymbol{I}+\boldsymbol{\nabla}\boldsymbol{P}_1\big]^{\mathrm{sym}}\Big\rangle \qquad \text{and} \qquad \boldsymbol{\mu}_2 = \Big\langle\mu\big[\boldsymbol{I}\otimes\boldsymbol{P}_2+\boldsymbol{\nabla}\boldsymbol{P}_3\big]^{\mathrm{sym}}\Big\rangle, \tag{4}$$

where the *second-order effective properties* $\boldsymbol{\varrho}_2$ and $\boldsymbol{\mu}_2$ are respectively a symmetric second-order tensor and a completely symmetric fourth-order tensor.

Remark 1. Each of the problems (3) can be interpreted as a compact tensorial writing of the *uncoupled* scalar problems that are satisfied by each component of $\boldsymbol{P}$. Practical methods to solve these scalar problems will be returned to in Section 3.1.

Second-order effective wave equation

The expansion (2) must be completed by a governing equation for the mean field U. At the second-order, the two-scale asymptotic analysis leads to the following *enriched* wave equation

$$\left(\boldsymbol{\mu}_0 + \ell^2\boldsymbol{\mu}_2 : \boldsymbol{\nabla}^2\right) : \boldsymbol{\nabla}^2 U + \omega^2\left(\varrho_0 + \ell^2\boldsymbol{\varrho}_2 : \boldsymbol{\nabla}^2\right)U = 0, \tag{5}$$

and in terms of the set of effective properties $\boldsymbol{m}_{\mathrm{eff}} = (\varrho_0, \boldsymbol{\mu}_0, \boldsymbol{\varrho}_2, \boldsymbol{\mu}_2)$ and the second and fourth-order gradient operators, and with $(\boldsymbol{\mu}_2 : \boldsymbol{\nabla}^2) : \boldsymbol{\nabla}^2 U = \boldsymbol{\mu}_2 :: \boldsymbol{\nabla}^4 U$. As this equation can be associated with a volumic energy $\mathcal{E}(U)$ given by

$$\mathcal{E}(U) = \frac{1}{2}\int_\Omega \left\{\boldsymbol{\nabla}U\cdot\boldsymbol{\mu}_0\cdot\boldsymbol{\nabla}U + \ell^2\boldsymbol{\nabla}^2U : \boldsymbol{\mu}_2 : \boldsymbol{\nabla}^2U + \omega^2\left(\varrho_0U^2 + \ell^2\boldsymbol{\nabla}U\cdot\boldsymbol{\varrho}_2\cdot\boldsymbol{\nabla}U\right)\right\}\mathrm{d}\boldsymbol{x},$$

i.e. of the type $\mathcal{E}(U) = \frac{1}{2}\int_\Omega\{\mathcal{W}(\boldsymbol{\nabla}U, \boldsymbol{\nabla}^2U) + \mathcal{K}(U, \boldsymbol{\nabla}U)\}\,\mathrm{d}\boldsymbol{x}$ with the strain energy density $\mathcal{W}$ and the kinetic energy density $\mathcal{K}$ being quadratic forms, it is typical of the so-called *second-gradient* materials, see *e.g.* [21,22].

Remark 2. The first-order coefficients $\boldsymbol{\varrho}_1 = \langle\rho\boldsymbol{P}_1\rangle$ and $\boldsymbol{\mu}_1 = \langle\mu[\boldsymbol{I}\otimes\boldsymbol{P}_1+\boldsymbol{\nabla}\boldsymbol{P}_2]^{\mathrm{sym}}\rangle$ also appear in the two-scale homogenization procedure, but their contributions to the cell problems (3) and to the wave equation (5) vanish for scalar waves, see [27].

To conclude, the homogeneous parameters in (4) constitute a set of *effective* material properties $\boldsymbol{m}_{\mathrm{eff}}$ that is entirely determined by the couple $(\boldsymbol{m}, Y)$ of constitutive properties and geometry of the reference cell that characterizes the considered composite material.

2.2 | Effective dispersive effects

The second-order effective wave equation (5) accounts for *anisotropic macroscopic dispersive effects* due to the microstructure. Indeed, taking U as a time-harmonic plane wave $U(\boldsymbol{x}) = e^{\mathrm{i}\boldsymbol{k}\cdot\boldsymbol{x}}$, with wavevector $\boldsymbol{k} = k\boldsymbol{\theta}$, where $k\in\mathbb{R}^+$ and the unit vector $\boldsymbol{\theta}$

will be referred to as the *wavenumber* and *direction* of the wave hereinafter, one obtains the dispersion relation:

$$\omega^2(k,\boldsymbol{\theta}) = k^2 \frac{\boldsymbol{\mu}_0 \,:\, \boldsymbol{\theta}^{\otimes 2} - \ell^2 k^2 \boldsymbol{\mu}_2 \,::\, \boldsymbol{\theta}^{\otimes 4}}{\varrho_0 - \ell^2 k^2 \boldsymbol{\varrho}_2 \,:\, \boldsymbol{\theta}^{\otimes 2}}, \tag{6}$$

where the notation $\boldsymbol{\theta}^{\otimes p}$ denotes p-th power of $\boldsymbol{\theta}$ owing to the tensorial product, see Appendix A.1.

Remark 3. From (6), the macroscopic wavelength mentioned above is straightforwardly defined as $\lambda = 2\pi/k$, and the asymptotic parameter that controls the relevance of the second-order approximation is indeed $k\ell = 2\pi\ell/\lambda = 2\pi\varepsilon$, *i.e.* the period-to-wavelength ratio (up to a constant factor). This justifies our choice to use the lengthscale ℓ rather than ε in the formal asymptotic expansion (2) for simplicity. Owing to this choice, the cell problems are defined directly on the unit cell Y rather than on *e.g.* "reference cells" $Y_\varepsilon = (\ell/\varepsilon)Y$. Other normalization choices are possible [19] but they do not impact the effective model (5), see also the related remark of [34].

The phase velocity $c(k,\boldsymbol{\theta}) = \omega(k,\boldsymbol{\theta})/k$ can accordingly be expanded as:

$$c(k,\boldsymbol{\theta}) = c_0(\boldsymbol{\theta}) + \frac{1}{2}\frac{d(\boldsymbol{\theta})}{c_0(\boldsymbol{\theta})}(k\ell)^2 + O((k\ell)^4) \tag{7}$$

In this expansion, c_0 is the *low-frequency limit velocity* that, owing to (6), satisfies

$$c_0(\boldsymbol{\theta}) = \sqrt{\frac{\boldsymbol{\mu}_0}{\varrho_0} \,:\, \boldsymbol{\theta}^{\otimes 2}}, \tag{8}$$

while the indicator $d(\boldsymbol{\theta})$, associated with the second-order dispersion term, is:

$$d(\boldsymbol{\theta}) = \left[\frac{\boldsymbol{\varrho}_2 \otimes \boldsymbol{\mu}_0 - \varrho_0 \boldsymbol{\mu}_2}{\varrho_0^2}\right]^{\mathrm{sym}} \,::\, \boldsymbol{\theta}^{\otimes 4}. \tag{9}$$

Similarly, the *group velocity* $c_g(k,\boldsymbol{\theta}) = \partial\omega(k,\boldsymbol{\theta})/\partial k$ can be expanded as:

$$c_g(k,\boldsymbol{\theta}) = c_0(\boldsymbol{\theta}) + \frac{3}{2}\frac{d(\boldsymbol{\theta})}{c_0(\boldsymbol{\theta})}(k\ell)^2 + O((k\ell)^4), \tag{10}$$

where the same coefficients c_0 and d/c_0 intervene.

In this study, the limit velocity $c_0(\boldsymbol{\theta})$ and the ratio $d(\boldsymbol{\theta})/c_0(\boldsymbol{\theta})$ are therefore chosen as characteristic indicators of the effective low-frequency dynamics of the second-order homogenized model (6) for waves propagating in direction $\boldsymbol{\theta}$.

Remark 4. The squared limit velocity $c_0^2(\boldsymbol{\theta})$ and the dispersion indicator $d(\boldsymbol{\theta})$ are respectively defined by (8) and (9) as quadratic and quartic functions of the coordinates $(\theta_1,\theta_2) = (\cos\theta, \sin\theta)$, in terms of completely symmetric tensors. Consequently, the representation of $c_0^2(\boldsymbol{\theta})$ in polar coordinates is an ellipse, *i.e.* $c_0^2(\boldsymbol{\theta})$ has at most one maximum and one minimum for $\theta \in [0,\pi]$, separated by $\Delta\theta = \pi/2$. Similarly, $d(\boldsymbol{\theta})$ has at most two local maxima and two local minima for $\theta \in [0,\pi]$, separated by $\Delta\theta = \pi/4$.

Remark 5. The ability of the second-order homogenized model to predict the effective dispersion due to the microstructure is supported by the comparison with the Bloch-wave homogenization method in the case $\rho = 1$, see *e.g.* [23,20,15]. It is notably proven that the second-order expansion (7) coincides with the one obtained when (ω, k) are the eigenfrequency and wavenumber associated with the first Bloch mode of the unit cell.

To our knowledge, these results have not been extended yet to the general case $\rho \neq 1$ which is considered here. However, in this case, the accuracy of the effective dispersion given by the second-order model is supported by (i) numerical computations of the exact and effective dispersion curves for particular microstructures [19,27,18] and (ii) comparison with other methods *e.g.* Willis' homogenization method [35].

2.3 | Optimization of the effective dynamics of waves

Objectives

On the basis of the second-order effective wave equation (5), we aim at generating numerically the spatial distribution of constitutive properties that characterize the microstructure of a composite in order to optimize its macroscopic dynamical properties $c_0(\boldsymbol{\theta})$ and $d(\boldsymbol{\theta})$ in (8-9) for a given wave propagation direction $\boldsymbol{\theta}$ or a set thereof. Therefore, we consider a *cost functional* $J\left(c_0, d\,;\boldsymbol{\theta}\right)$ to be minimized, a functional that can be formally expressed in terms of the effective parameters as $J\left(c_0, d\,;\boldsymbol{\theta}\right) \equiv J\left(\boldsymbol{m}_{\mathrm{eff}};\boldsymbol{\theta}\right)$.

As the set $\boldsymbol{m}_{\text{eff}} = (\varrho_0, \boldsymbol{\mu}_0, \boldsymbol{\varrho}_2, \boldsymbol{\mu}_2)$ itself depends on the constitutive properties $\boldsymbol{m} = (\rho, \mu)$ at the microscopic level and on the geometry of the unit cell Y, we consider the following optimization problem:

$$\text{Compute} \quad \boldsymbol{m}_{\text{opt}} = \arg\min_{\boldsymbol{m}} \mathcal{J}(\boldsymbol{m}, Y) \quad \text{where} \quad \mathcal{J}(\boldsymbol{m}, Y) = J(\boldsymbol{m}_{\text{eff}}\,; \boldsymbol{\theta}). \tag{11}$$

Note that the computation of the set $\boldsymbol{m}_{\text{opt}} = (\rho_{\text{opt}}, \mu_{\text{opt}})$ of some optimal material property distributions within Y that achieve the sought objective can possibly be performed under some relevant constrains or material admissibility conditions. These contraints may also reduce the search perimeter and help avoiding some of the local minima of the (most often) non-convex cost functionals. Specific examples of cost functionals are investigated in Section 4.

Topological optimization

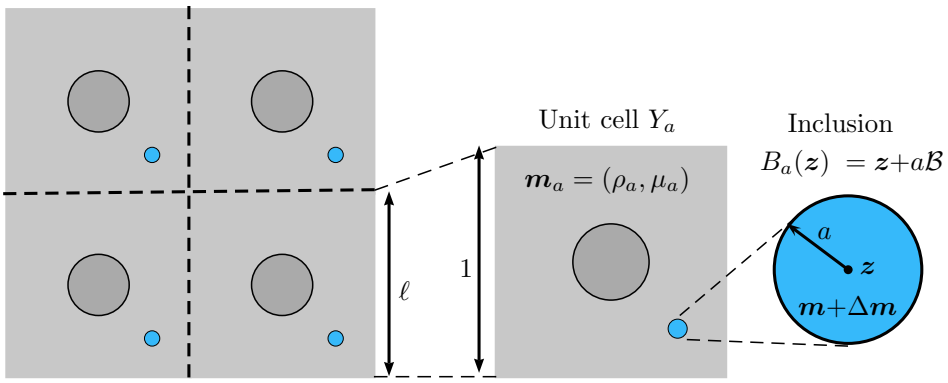

FIGURE 2 Perturbed periodic medium and unit cell Y_a, and inhomogeneity B_a.

To tackle the optimization problem (11), we allow *topological perturbations* of the microstructure. Such a perturbation is depicted in Figure 2: an inhomogeneity $B_a = \boldsymbol{z} + a\mathcal{B}$ of shape $\mathcal{B}$ and size a is placed at point $\boldsymbol{z} \in Y$. It supports a *constant* material perturbation $\Delta\boldsymbol{m} = (\Delta\rho, \Delta\mu)$, so that the constitutive properties that characterize the *perturbed* composite are

$$\boldsymbol{m}_a = (\rho_a, \mu_a) = \big(\rho + \Delta\rho\, \chi_{B_a}, \mu + \Delta\mu\, \chi_{B_a}\big),$$

where χ_{B_a} denotes the characteristic function of the nucleating inhomogeneity B_a. In this context the cost functional $\mathcal{J}$ is said to admit a *topological derivative* (or *gradient*) denoted as $\mathcal{D}\mathcal{J}$ [36,25,27] if, in the limit of an infinitesimal topological perturbation of the microstructure, *i.e.* when $a \to 0$, the following expansion of the perturbed cost functional $\mathcal{J}(\boldsymbol{m}_a, Y)$ holds:

$$\mathcal{J}(\boldsymbol{m}_a, Y) \underset{a\to 0}{=} \mathcal{J}(\boldsymbol{m}, Y) + \frac{a^2}{|Y|}\mathcal{D}\mathcal{J}(\boldsymbol{m}, Y; \boldsymbol{z}, \mathcal{B}, \Delta\boldsymbol{m}) + o(a^2). \tag{12}$$

The topological derivative provides information on the influence of a given perturbation on the unit cell, *e.g.* for fixed shape $\mathcal{B}$ and material perturbation $\Delta\boldsymbol{m}$, the most negative (resp. positive) values of the map $\boldsymbol{z} \mapsto \mathcal{D}\mathcal{J}(\boldsymbol{m}, Y; \boldsymbol{z}, \mathcal{B}, \Delta\boldsymbol{m})$ indicate the locations where the localized perturbation $\Delta\boldsymbol{m}$ would effectively decrease (resp. increase) the cost functional.

Remark 6. The choice of the scaling coefficient $a^2/|Y|$ in (12) is made for convenience in the present context (remind that $|Y| = 1$ for square cells and $|Y| = O(1)$ otherwise). Other choices of scaling are possible, *e.g.* just a^2 or the surface fraction $|B_a|/|Y| = a^2|\mathcal{B}|/|Y|$. The forthcoming topological derivatives to be discussed hereafter must be modified accordingly.

Since the cost functional J is formulated in terms of the set $\boldsymbol{m}_{\text{eff}} = (\varrho_0, \boldsymbol{\mu}_0, \boldsymbol{\varrho}_2, \boldsymbol{\mu}_2)$ of effective parameters, if J is differentiable with respect to these parameters, then the topological derivative of $\mathcal{J}$ is computed with the classical chain rule as:

$$\mathcal{D}\mathcal{J} = \frac{\partial J}{\partial \varrho_0}\mathcal{D}\varrho_0 + \frac{\partial J}{\partial \boldsymbol{\mu}_0} : \mathcal{D}\boldsymbol{\mu}_0 + \frac{\partial J}{\partial \boldsymbol{\varrho}_2} : \mathcal{D}\boldsymbol{\varrho}_2 + \frac{\partial J}{\partial \boldsymbol{\mu}_2} :: \mathcal{D}\boldsymbol{\mu}_2, \tag{13}$$

where the topological derivatives $(\mathcal{D}\varrho_0, \mathcal{D}\boldsymbol{\mu}_0, \mathcal{D}\boldsymbol{\varrho}_2, \mathcal{D}\boldsymbol{\mu}_2)$ of the effective parameters, which appear at the right-hand side of the above identity, are defined as in (12).

Remark 7. Hereinafter, only the dependence of the topological derivatives on the perturbation location $\boldsymbol{z}$ is kept for brevity, *i.e.* $\mathcal{D}\mathcal{J}(\boldsymbol{z}) = \mathcal{D}\mathcal{J}(\boldsymbol{m}, Y; \boldsymbol{z}, \mathcal{B}, \Delta\boldsymbol{m})$. The choice of the perturbation shape $\mathcal{B}$ and contrast $\Delta\boldsymbol{m}$ will be specified explicitly when needed.

Topological derivatives of effective parameters

The computation the topological derivative (13) involves these of the homogenized coefficients. The latter were computed in [27], under the assumption that ρ and μ are smooth at the nucleation point $\boldsymbol{z}$ (in particular, $\boldsymbol{z}$ should lie away of any material interface within Y). Their expressions are discussed below for the reader's convenience. At the zero-th order one has:

$$\mathcal{D}\varrho_0(\boldsymbol{z}) = |\mathcal{B}|\Delta\rho, \qquad \mathcal{D}\boldsymbol{\mu}_0(\boldsymbol{z}) = \frac{1}{\mu(\boldsymbol{z})^2}\boldsymbol{S}_0(\boldsymbol{z})^{\mathrm{T}} \cdot \boldsymbol{A}(\boldsymbol{z}) \cdot \boldsymbol{S}_0(\boldsymbol{z}), \tag{14}$$

where the cell stresses $\boldsymbol{S}_j$ are defined as $\boldsymbol{S}_j(\boldsymbol{y}) = \mu(\boldsymbol{y})\left[\boldsymbol{E}_{j+1}(\boldsymbol{y}) + \boldsymbol{\nabla}\boldsymbol{P}_{j+1}(\boldsymbol{y})\right]$ for all $j \in \{0, 1, 2\}$ based on Equation (3) and Table 1. In the above formula, $\boldsymbol{A}$ is the *polarization tensor*[37] of the inclusion, that depends on the reference shape $\mathcal{B}$, on the background shear modulus $\mu(\boldsymbol{z})$ at the nucleation point and on the modulus perturbation $\Delta\mu$. It is known analytically for simple shapes, while for arbitrary shapes it can be computed by solving a *free-space transmission problem*, e.g. using integral equations and boundary elements. To be used later on, we recall the following expressions when $\mathcal{B}$ is the unit disc, see [37]:

$$|\mathcal{B}^{\mathrm{disc}}| = \pi \quad \text{and} \quad \boldsymbol{A}^{\mathrm{disc}}(\boldsymbol{z}) = 2\pi\mu(\boldsymbol{z})\frac{\Delta\mu}{2\mu(\boldsymbol{z}) + \Delta\mu}\boldsymbol{I}. \tag{15}$$

Moreover, for the second-order parameter $\boldsymbol{\varrho}_2$ it holds

$$\begin{aligned}\mathcal{D}\boldsymbol{\varrho}_2(\boldsymbol{z}) = \frac{\varrho_0}{\mu(\boldsymbol{z})}\Big\{ -\left(\beta_0\boldsymbol{I} + \boldsymbol{\nabla}\boldsymbol{\beta}_1\right) \cdot \boldsymbol{A} \cdot \boldsymbol{S}_0 + \boldsymbol{\nabla}\beta_0 \cdot \boldsymbol{A} \cdot \boldsymbol{S}_1 \Big\}^{\mathrm{sym}}(\boldsymbol{z}) \\ + \left\{ \mathcal{D}\varrho_0\left(\boldsymbol{P}_2 + \beta_0\boldsymbol{\mu}_0\right) + \langle\rho\beta_0\rangle\left(\mathcal{D}\boldsymbol{\mu}_0 - \frac{\mathcal{D}\varrho_0}{\varrho_0}\boldsymbol{\mu}_0\right) \right\}^{\mathrm{sym}}(\boldsymbol{z}).\end{aligned} \tag{16}$$

In this formula, $\mathcal{D}\boldsymbol{\varrho}_2$ is expressed thanks to two additional *adjoint cell functions* β_0 and $\boldsymbol{\beta}_1$, which are respectively a scalar and a vector field defined as the solutions to (3) for the prestrains $\boldsymbol{E}$ and body forces $\boldsymbol{f}$ given in Table 2

Cell function $\boldsymbol{P}$	Prestrain $\boldsymbol{E}$	Body force $\boldsymbol{f}$
β_0	$\boldsymbol{0}$	$1 - (\rho/\varrho_0)$
$\boldsymbol{\beta}_1$	$\beta_0\boldsymbol{I}$	$\mu\boldsymbol{\nabla}\beta_0$

TABLE 2 Notations and values of the prestrain and body force for the adjoint cell problems.

Remark 8. From Table 2, the definitions of β_0 and $\boldsymbol{\beta}_1$ have been slightly modified compared to their counterparts denoted β and $\boldsymbol{X}[\beta]$ in a previous work [27]: one has $\beta_0 = -\beta/\varrho_0$ and $\boldsymbol{\beta}_1 = \boldsymbol{X}[\beta]/\varrho_0$. The expression (16) of the topological derivative $\mathcal{D}\boldsymbol{\varrho}_2$ was modified accordingly.

Lastly, the topological derivative of the fourth-order tensor $\boldsymbol{\mu}_2$ is given by:

$$\begin{aligned}\mathcal{D}\boldsymbol{\mu}_2(\boldsymbol{z}) = \frac{1}{\mu(\boldsymbol{z})^2}\left\{2\boldsymbol{S}_0^{\mathrm{T}} \cdot \boldsymbol{A} \cdot \boldsymbol{S}_2 - \boldsymbol{S}_1^{\mathrm{T}} \cdot \boldsymbol{A} \cdot \boldsymbol{S}_1\right\}^{\mathrm{sym}}(\boldsymbol{z}) \\ + \frac{1}{\varrho_0}\left\{ \left[\mathcal{D}\boldsymbol{\varrho}_2 + \mathcal{D}\varrho_0\left(\boldsymbol{P}_1^{\otimes 2} - 2\boldsymbol{P}_2\right)\right] \otimes \boldsymbol{\mu}_0 + \left(\left\langle\rho\boldsymbol{P}_1^{\otimes 2}\right\rangle - \boldsymbol{\varrho}_2\right) \otimes \left(\mathcal{D}\boldsymbol{\mu}_0 - \frac{\mathcal{D}\varrho_0}{\varrho_0}\boldsymbol{\mu}_0\right) \right\}^{\mathrm{sym}}(\boldsymbol{z}).\end{aligned} \tag{17}$$

3 | A FAST TOPOLOGICAL OPTIMIZATION APPROACH

The aim of an optimization algorithm is to compute an optimal composite material is the sense of (11). To achieve this numerically, the set of material properties and the geometry of the cell are both discretized using suitable bases. This question will be returned to hereafter and the quantities that are involved in the formal algorithm below are to be understood as discrete ones. For a given cost functional $\boldsymbol{J}(\boldsymbol{m}_{\mathrm{eff}}; \boldsymbol{\theta})$, a topological derivative-based iterative algorithm is given by Algorithm 1 below.

Algorithm 1 Topological derivative-based algorithm to optimize the composite effective dynamics

I. *Initialization:*

1. Define the unit cell geometry Y and the initial constitutive properties $\boldsymbol{m}^{(0)} = (\rho^{(0)}, \mu^{(0)})$.
2. Define the admissible topological and material perturbations $\mathcal{B}$ and $\Delta\boldsymbol{m} = (\Delta\rho, \Delta\mu)$.
3. Define a stopping criterion.

II. *Then:* iterate until convergence

1. Compute the cell functions $(\boldsymbol{P}_1^{(n)}, \boldsymbol{P}_2^{(n)}, \boldsymbol{P}_3^{(n)}, \beta_0^{(n)}, \boldsymbol{\beta}_1^{(n)})$ for the unit cell characterized by $(\boldsymbol{m}^{(n)}, Y)$.
2. Compute the topological derivatives of the effective properties $\boldsymbol{m}_{\mathrm{eff}}^{(n)}$, *i.e.* $\mathcal{D}\varrho_0^{(n)}, \mathcal{D}\boldsymbol{\mu}_0^{(n)}, \mathcal{D}\boldsymbol{\varrho}_2^{(n)}, \mathcal{D}\boldsymbol{\mu}_2^{(n)}$, and the cost functional topological derivative $\mathcal{D}\mathcal{J}^{(n)}$.
3. Update the material properties to $\boldsymbol{m}^{(n+1)} = \left(\rho^{(n+1)}, \mu^{(n+1)}\right)$ based on the information provided by the map $\boldsymbol{z} \mapsto \mathcal{D}\mathcal{J}^{(n)}(\boldsymbol{z})$, see Algorithm 2.

The step II.1 requires to solve five cell problems given the current material configuration $\boldsymbol{m}^{(n)}$ of the composite. To do so, an efficient numerical method is required and this issue is discussed in detail in Section 3.1 below. The updating step II.3 is crucial to the efficiency of the whole method. Moreover, it is possibly constrained by the choice of the overall numerical approach adopted, and in particular on the discretization considered. For the case of two-phase materials, some possibilities are discussed in Section 3.2.

3.1 | FFT-based computations of cell functions

The direct cell functions $\{\boldsymbol{P}_j\}_{j=1,2,3}$ and their adjoint counterparts β_0, $\boldsymbol{\beta}_1$ are all expressed as the solutions of the generic cell problem (3) for the specific source terms that are reported in the tables 1 and 2 respectively. Owing to (3.ii) and the definitions of Appendix A.1, the equilibrium equation (3.iii) is a tensor-valued local equation that can be expanded as:

$$\operatorname{div}(\mu(\boldsymbol{y})\boldsymbol{E}(\boldsymbol{y})) + \sum_{i=1}^{2} \frac{\partial}{y_i}\left(\mu(\boldsymbol{y})\frac{\partial \boldsymbol{P}(\boldsymbol{y})}{\partial y_i}\right) + \boldsymbol{f}(\boldsymbol{y}) = \boldsymbol{0}.$$

Therefore, each component of that equation involves the partial derivatives of only the corresponding component of the unknown tensor $\boldsymbol{P}$. As a consequence, the cell problem (3) can be solved independently for each of the components of the direct and adjoint cell functions. Note that the second-order tensor $\boldsymbol{P}_2$ and the third-order tensor $\boldsymbol{P}_3$ being symmetric, one only has to determine their independent components $(P_2)_{11}, (P_2)_{12}, (P_2)_{22}$ and $(P_3)_{111}, (P_3)_{112}, (P_3)_{122}, (P_3)_{222}$ for the 2D setting considered .

Based on the above argument, one focuses in this section on a computational approach to solve the generic cell problem (3) in the case where the unknown is a *scalar*-valued function P (and so is the body force f). Solving this problem numerically may be done in several ways: one of them is the Finite Elements Method (FEM), in which case the equivalent weak form of the problem (3) is needed, see *e.g.*[27]. Here, we make use of the method introduced in[28] for the computational homogenization of periodic composites. The specificity of the latter is to employ a Fourier-based formulation to solve (3) and to seek numerical efficiency through an intensive use of the Fast Fourier Transform (FFT). We describe this approach below.

Considering a reference comparison medium characterized by the constant modulus μ_*, then $\boldsymbol{S}$ in (3.ii) is rewritten as

$$\boldsymbol{S}(\boldsymbol{y}) = \mu_* \boldsymbol{\nabla} P(\boldsymbol{y}) + \boldsymbol{T}(\boldsymbol{y}) \qquad \text{with} \qquad \boldsymbol{T}(\boldsymbol{y}) = \mu(\boldsymbol{y})\boldsymbol{E}(\boldsymbol{y}) + \delta\mu(\boldsymbol{y})\boldsymbol{\nabla} P(\boldsymbol{y}), \tag{18}$$

where $\delta\mu(\boldsymbol{y}) = \mu(\boldsymbol{y}) - \mu_*$. Considering an auxiliary problem of the form (3) with (3.ii) being replaced by (18), i.e. with $\boldsymbol{T}$ defined above serving as the source term in addition to the body force f, then making use of the Fourier transform (see Appendix A.2) leads to the following identities in the Fourier space

$$\begin{cases} \hat{P}(\boldsymbol{0}) = 0, \\ \hat{P}(\boldsymbol{\xi}) = \dfrac{1}{\mu_* |\boldsymbol{\xi}|^2}\left(\hat{f}(\boldsymbol{\xi}) + \mathrm{i}\boldsymbol{\xi} \cdot \hat{\boldsymbol{T}}(\boldsymbol{\xi})\right) \qquad \forall \boldsymbol{\xi} \in \mathcal{R}^* \setminus \{\boldsymbol{0}\}. \end{cases} \tag{19}$$

Substituting the expression for $\boldsymbol{T}$ back into (19) yields the following equation for the field P:

$$P(\boldsymbol{y}) = \mathcal{G}_*\big[f + \operatorname{div}\left(\mu \boldsymbol{E} + \delta\mu \boldsymbol{\nabla} P\right)\big](\boldsymbol{y}). \tag{20}$$

where $\mathcal{G}_*$ is the periodic differential operator formally defined as $\mathcal{G}_* = -(\mu_* \Delta)^{-1}$, in terms of the Laplace operator, which is such that for all $(h, \boldsymbol{g}) \in L^2_{\text{per}}(Y) \times \boldsymbol{L}^2_{\text{per}}(Y)$ it holds

$$\mathcal{G}_* h(\boldsymbol{y}) = \mathscr{F}^{-1}\left[(\mu_* |\boldsymbol{\xi}|^2)^{-1} \mathscr{F}[h]\right](\boldsymbol{y}) \qquad \text{and} \qquad \mathcal{G}_* \operatorname{div} \boldsymbol{g}(\boldsymbol{y}) = \mathscr{F}^{-1}\left[(\mu_* |\boldsymbol{\xi}|^2)^{-1} \mathrm{i}\boldsymbol{\xi} \cdot \mathscr{F}[\boldsymbol{g}]\right](\boldsymbol{y}). \tag{21}$$

The equation (20) is then solved by the following fixed-point scheme:

$$\begin{cases} P^{(0)}(\boldsymbol{y}) = 0, \\ P^{(n+1)}(\boldsymbol{y}) = \mathcal{G}_*\left[f + \operatorname{div}\left(\mu \boldsymbol{E} + \delta\mu \boldsymbol{\nabla} P^{(n)}\right)\right](\boldsymbol{y}). \end{cases} \tag{22}$$

In the scheme (22), the action of the featured differential operators is computed *locally* in the Fourier space, *i.e.* algebraically for each frequency $\boldsymbol{\xi} \in \mathcal{R}^* \setminus \{\boldsymbol{0}\}$ based on the identities (21). Moreover, multiplication by the material property μ or by the contrast $\delta\mu$ is performed *locally* in the physical space. Therefore, in the above algorithm one alternates back and forth between the physical space and the Fourier space while taking full advantage of the FFT to do so for computational efficiency. The above fixed-point iterations are conditionally convergent and convergence is expected when the reference medium μ_* is appropriately chosen. By extending the arguments of[28] to the present formulation one sets $\mu_* = (\max_Y \mu + \min_Y \mu)/2$.

The stopping criterion adopted in this work is:

$$\frac{\|\boldsymbol{P}_j^{(n+1)} - \boldsymbol{P}_j^{(n)}\|_{L^2(Y)}}{\|\boldsymbol{P}_j^{(n)}\|_{L^2(Y)}} < \varepsilon_{\text{FP}}, \tag{23}$$

i.e. the fixed-point algorithm is applied simultaneously on each component of $\boldsymbol{P}_j$ and the relative residual of the full cell function (or adjoint cell function) is compared to a user-defined tolerance ε_{FP}. Other choices are possible, see[38] and the references therein.

The Fourier-based approach adopted to solve the cell problems is limited by the convergence rate of the fixed-point iterations, which is proportional to the normalized contrast $\delta\mu/\mu_*$. Moreover, unlike in the FEM, local refinement is not permitted, which could lead to imperfect geometrical discretizations of interfaces. Despite these limits, this method is relatively easy to implement. It is a meshless method, by opposition to the FEM, in that it uses a discretization of the period cell of the composite considered into a set of pixels. It can be easily generalized to 3D configurations while the use of the FFT makes it numerically efficient in any dimension. Note that alternative algorithms exist for highly-contrasted composites[39,40] and that nonlinear material behaviors can also be handled with this approach[28].

3.2 | Material updating step for two-phase composites

From now on, we restrain ourselves to two-phase composites: the unit cell is composed of two materials filling the phase domains Y_A and Y_B such that

$$Y = Y_A \cup Y_B \qquad \text{with} \qquad Y_A \cap Y_B = \emptyset,$$

and characterized by the material parameters $\boldsymbol{m}_A = (\rho_A, \mu_A)$ and $\boldsymbol{m}_B = (\rho_B, \mu_B)$, respectively. Upon defining the contrast between phases as $\Delta\boldsymbol{m}_{AB} = \boldsymbol{m}_B - \boldsymbol{m}_A = (\rho_B - \rho_A, \mu_B - \mu_A)$, which is a pair of uniform fields, then the set of constitutive properties reduces to:

$$\boldsymbol{m} = \boldsymbol{m}_A + \chi_B \Delta\boldsymbol{m}_{AB} = \big(\rho_A + \chi_B \Delta\rho_{AB},\ \mu_A + \chi_B \Delta\mu_{AB}\big), \qquad \chi_B = \chi_{Y_B}.$$

Moreover, the only material modification allowed in the optimization process is a *phase conversion*. Accordingly, the material perturbation $\Delta\boldsymbol{m}$ featured in the topological derivative (12) is chosen as:

$$\Delta\boldsymbol{m} = \Delta\boldsymbol{m}_{AB} \text{ in } Y_A \qquad \text{and} \qquad \Delta\boldsymbol{m} = -\Delta\boldsymbol{m}_{AB} \text{ in } Y_B. \tag{24}$$

Lastly, the unit cell Y is discretized into a uniform grid of $N \times N$ pixels in order to make use of the FFT-based solver presented in Section 3.1 for the computation of the cell problems. In this setting, three updating strategies are discussed hereafter but without making an explicit use of such a discretization.

3.2.1 | Pixel-by-pixel update of the unit cell

At a given iteration n, one considers the subset $Y^- \subset Y$ of the unit cell where the topological derivative map $\boldsymbol{z} \mapsto \mathcal{D}\mathcal{J}^{(n)}(\boldsymbol{z})$ is negative, *i.e.*

$$Y^- = \Big\{ \boldsymbol{z} \in Y \ : \ \mathcal{D}\mathcal{J}^{(n)}(\boldsymbol{z}) < 0 \Big\}.$$

Doing so, the simplest update one may think of is the following: a phase conversion is applied to the point (*i.e.* pixel) $\boldsymbol{z}_p$ where $\mathcal{D}\mathcal{J}^{(n)}$ is the most negative, i.e.

$$\boldsymbol{z}_p = \underset{\boldsymbol{z} \in Y^-}{\arg\min}\, \mathcal{D}\mathcal{J}^{(n)}(\boldsymbol{z}).$$

Alternatively, if the phase ratio is initially fixed in the optimization problem, one may "exchange" the materials at two points $\boldsymbol{z}_{pA}$ and $\boldsymbol{z}_{pB}$ that respectively belongs to the phase Y_A and Y_B. To do so, one introduces the two-phase subset $Y^-_{AB} \subset Y_A \times Y_B$ as

$$Y^-_{AB} = \Big\{ (\boldsymbol{z}_A, \boldsymbol{z}_B) \in Y_A \times Y_B \ : \ \big(\mathcal{D}\mathcal{J}^{(n)}(\boldsymbol{z}_A) + \mathcal{D}\mathcal{J}^{(n)}(\boldsymbol{z}_B)\big) < 0 \Big\}.$$

and exchange the materials at the pair of points $(\boldsymbol{z}_{pA}, \boldsymbol{z}_{pB}) \in Y_A \times Y_B$ such that

$$(\boldsymbol{z}_{pA}, \boldsymbol{z}_{pB}) = \underset{(\boldsymbol{z}_A, \boldsymbol{z}_B) \in Y^-_{AB}}{\arg\min} \ \big(\mathcal{D}\mathcal{J}^{(n)}(\boldsymbol{z}_A) + \mathcal{D}\mathcal{J}^{(n)}(\boldsymbol{z}_B)\big).$$

For these pixel-by-pixel updating strategies, the corresponding stopping criteria are defined as:

$$\begin{cases} \min\limits_{Y} \mathcal{D}\mathcal{J}^{(n)} \geq 0 & \textit{i.e. } Y^- = \emptyset \quad \text{for the one-pixel phase permutation,} \\ \min\limits_{Y_A} \mathcal{D}\mathcal{J}^{(n)} + \min\limits_{Y_B} \mathcal{D}\mathcal{J}^{(n)} \geq 0 & \textit{i.e. } Y^-_{AB} = \emptyset \quad \text{for the two-pixel exchange.} \end{cases} \tag{25}$$

A similar procedure is proposed by [12] that uses finite elements instead of pixels to discretize the cell. As it will be illustrated by the upcoming numerical examples, this technique is very simple to implement, and is observed on these examples to be efficient at reducing the value of the cost functional $\mathcal{J}$ at each iteration. However, this method has two major drawbacks, namely (i) there is no theoretical guarantee that the cost functional will monotonically decrease, and (ii) the whole process may be very slow if the initalization is far from the optimal microstructure, and especially when a fine discretization is required (*e.g.* when one expects a complex optimal microstructure). It is why we also use another level-set based algorithm presented now.

3.2.2 | Level-set representation and projection onto the topological derivative

A common way to characterize a two-phase material distribution is to use a *level-set function*, *i.e.* a function ψ satisfying:

$$\begin{cases} \psi(\boldsymbol{z}) > 0 & \text{in } Y_A \\ \psi(\boldsymbol{z}) < 0 & \text{in } Y_B \end{cases} \qquad \text{and} \qquad \|\psi\|_{L^2(Y)} = 1. \tag{26}$$

Accordingly, for the two-phase composite described in the preamble of this section, a level-set function ψ entirely determine the material distribution $\boldsymbol{m}$. Then, updating ψ may be achieved by several ways. A widely used update method relies on a Hamilton-Jacobi equation that allows the interface between phases, which corresponds to the level-set $\psi(\boldsymbol{z}) = 0$, to evolve based on the knowledge of the *shape derivative* of the cost functional $\mathcal{J}$ with respect to a perturbation of this interface, see *e.g.* [41,15]. Since we consider here only topological perturbation, we use instead the projection algorithm proposed by [42], theoretically analyzed in [26] and that has been used since then in ensuing studies *e.g.* [13,43,14].

Let us first defines the *signed* normalized topological derivative $\overline{\mathcal{D}}\mathcal{J}^{(n)}$ at a given iteration n as:

$$\overline{\mathcal{D}}\mathcal{J}^{(n)}(\boldsymbol{z}) \overset{\text{def}}{=} \begin{cases} \mathcal{D}\mathcal{J}^{(n)}(\boldsymbol{z}) \,/\, \|\mathcal{D}\mathcal{J}^{(n)}\|_{L^2(Y)} & \text{in } Y_A \\ -\mathcal{D}\mathcal{J}^{(n)}(\boldsymbol{z}) \,/\, \|\mathcal{D}\mathcal{J}^{(n)}\|_{L^2(Y)} & \text{in } Y_B \end{cases} \qquad \text{so that } \|\overline{\mathcal{D}}\mathcal{J}^{(n)}\|_{L^2(Y)} = 1. \tag{27}$$

A *sufficient optimality condition* for a topological gradient-based minimization scheme is then obtained when $\overline{\mathcal{D}}\mathcal{J}^{(n)}$ satisfies the sign conditions (26). Indeed, in this case, the definition (27) entails that $\mathcal{D}\mathcal{J}^{(n)}(\boldsymbol{z}) > 0$ in the whole cell Y, *i.e.* the value of the cost functional $\mathcal{J}$ (or rather its leading-order approximation (12)) cannot be decreased anymore by an infinitesimal phase change. This optimality condition therefore ensure that the material configuration corresponds to a local minimum of $\mathcal{J}$.

The level-set update proposed in [42] aims at fulfilling this optimality condition: at each iteration, the new level-set function $\psi^{(n+1)}$ is defined as the following linear combination of its previous value $\psi^{(n)}$ and of the signed topological derivative $\overline{\mathcal{D}}\mathcal{J}^{(n)}$:

$$\psi^{(n+1)}(\boldsymbol{z}) = \frac{1}{\sin\left(\Theta^{(n)}\right)} \left[\sin\left(\left(1 - \kappa^{(n)}\right)\Theta^{(n)}\right) \psi^{(n)}(\boldsymbol{z}) + \sin\left(\kappa^{(n)}\Theta^{(n)}\right) \overline{\mathcal{D}}\mathcal{J}^{(n)}(\boldsymbol{z}) \right], \tag{28}$$

where $\kappa^{(n)} \in [0,1]$ while $\Theta^{(n)}$ is an angle computed using the standard scalar product on $L^2(Y)$ as:

$$\Theta^{(n)} \stackrel{\text{def}}{=} \cos^{-1}\left(\overline{\mathcal{D}}\mathcal{J}^{(n)}, \psi^{(n)}\right)_{L^2(Y)}. \tag{29}$$

According to (28), the level set function is updated using a partial projection of $\psi^{(n)}$ onto $\overline{\mathcal{D}}\mathcal{J}^{(n)}$, weighted by the parameter $\kappa^{(n)}$. This parameter ensures that the cost functional $\mathcal{J}$ decreases at each iteration. In practice, it is determined within an inner optimization loop: it is initialized to $\kappa^{(n)} = \min(1, 2\kappa^{(n-1)})$, where $\kappa^{(n)} = 1$ means that the next level-set function is set to $\psi^{(n+1)}(\boldsymbol{z}) = \overline{\mathcal{D}}\mathcal{J}^{(n)}(\boldsymbol{z})$, and then $\kappa^{(n)}$ is reduced towards a minimum value $\kappa_{\min}$ if the resulting value of the cost-functional $\mathcal{J}\left(\boldsymbol{m}^{(n+1)}, Y\right)$ increases.

The overall stopping criterion associated with the updating process (28) for the level-set function is chosen as:

$$|\Theta^{(n)}| < \varepsilon_{\text{LS}}, \tag{30}$$

where ε_{LS} is a user-defined tolerance.

3.2.3 | Mixed algorithm

We observed on some examples that the level-set algorithm fails at decreasing the cost functional value with $\kappa^{(n)} > \kappa_{\min}$, while a pixel conversion would still decrease this value. To leave both options open, we therefore keep both tools and propose a simple two-step algorithm. First, we use the level-set projection until (i) the criterion (30) is satisfied or (ii) the value of $\mathcal{J}$ cannot be decreased by the update (28) for any $\kappa^{(n)} > \kappa_{\min}$. In the case (i), a local minimum is reached and we stop the procedure. In the case (ii), we try to further improve the resulting miscrostructure by applying the pixel-by-pixel update until the stopping criterion (25) is satisfied. The pixel-by-pixel update is also stopped when a phase change is applied twice to the same pixel, *i.e.* when $|\mathcal{J}\left(\boldsymbol{m}^{(n+1)}, Y\right) - \mathcal{J}\left(\boldsymbol{m}^{(n-1)}, Y\right)| < \varepsilon_{\text{pixel}}$ with $\varepsilon_{\text{pixel}}$ a tolerance close to the machine precision. This mixed algorithm, which constitute the material updating step II.3 of the overall topological optimization algorithm 1 is summarized below.

Algorithm 2 Material updating step II.3 of Algorithm 1

II.3.1 *Initialization:*

(a) The material distribution $\boldsymbol{m}^{(n)}$ with its level-set representation $\psi^{(n)}$ are available at step II

(b) The topological derivative $\mathcal{D}\mathcal{J}^{(n)}(\boldsymbol{z})$ is available from step II.2

(c) Choose the tolerances ε_{LS} and $\varepsilon_{\text{pixel}}$ and the minimum value $\kappa_{\min}$

II.3.2 *Then:* Level-set update to compute globally the distribution $\boldsymbol{m}^{(n+1)}$ using the function $\psi^{(n+1)}$

(a) Compute the normalized signed topological derivative $\overline{\mathcal{D}}\mathcal{J}^{(n)}(\boldsymbol{z})$ from (27)

(b) Compute the projection angle $\Theta^{(n)}$ from (29)

(c) If $|\Theta^{(n)}| < \varepsilon_{\text{LS}}$ then $\psi^{(n+1)}(\boldsymbol{z}) = \overline{\mathcal{D}}\mathcal{J}^{(n)}(\boldsymbol{z})$ and step II.3 is ended
else set $\kappa^{(n)} = \min(1, 2\kappa^{(n-1)})$ and compute $\psi^{(n+1)}(\boldsymbol{z})$ from (28)

(d) While $\mathcal{J}\left(\boldsymbol{m}^{(n+1)}, Y\right) > \mathcal{J}\left(\boldsymbol{m}^{(n)}, Y\right)$ do:
- set $\kappa^{(n)} \leftarrow \kappa^{(n)}/2$
- if $\kappa^{(n)} < \kappa_{\min}$ then go to II.3.3 as $\mathcal{J}$ cannot be decreased by the level-set projection
else recompute $\psi^{(n+1)}(\boldsymbol{z})$ from (28)

II.3.3 Pixel-by-pixel update to modify locally the distribution $\boldsymbol{m}^{(n+1)}$ obtained from II.3.2(d)

(a) Compute the topological derivative $\mathcal{D}\mathcal{J}^{(n+1)}$

(b) While stopping criterion (25) is not met and $|\mathcal{J}\left(\boldsymbol{m}^{(n+1)}, Y\right) - \mathcal{J}\left(\boldsymbol{m}^{(n-1)}, Y\right)| > \varepsilon_{\text{pixel}}$ do:
- apply a pixel-by-pixel update to $\boldsymbol{m}^{(n+1)}$

4 | NUMERICAL EXAMPLES

In this section, we discuss a number of numerical examples of microstructure optimizations. Each example is associated with a specific cost functional to be minimized and the results obtained by applying the topological gradient-based algorithm of the previous section are then presented. Note that, in the examples discussed hereafter, the topological derivatives are defined at the continuous level for a material perturbation $\Delta \boldsymbol{m}$ given by (24) and an infinitesimal circular perturbation $\boldsymbol{B}_a$, so that expression (15) of the polarization tensor $\boldsymbol{A}$ is employed in the formulas (14), (16) and (17). The numerical values of the parameters associated with the algorithms presented in the previous section are provided in Table 3.

ε_{FP}	$\kappa_{\min}$	ε_{LS}	$\varepsilon_{\text{pixel}}$
10^{-8}	10^{-3}	10^{-3}	10^{-10}

TABLE 3 Parameters of the fixed-point and topological optimisation algorithms used in the numerical examples.

4.1 | Maximizing the dispersion in given directions

As a first example, we aim at maximizing or minimizing the effective dispersion in N_θ directions of interest $\boldsymbol{\theta}_j = (\cos\theta_j, \sin\theta_j)_{j=1..N_\theta}$. To this end, on the basis of the second-order dispersive terms in the expansions of the phase and group velocities (7) and (10), which are both driven by the ratio d/c_0, we introduce the quadratic cost functional:

$$J(\boldsymbol{\theta}_1, \boldsymbol{\theta}_2, \dots, \boldsymbol{\theta}_{N_\theta}) = \frac{1}{2} \sum_{j=1}^{N_\theta} w_j \left(\frac{d(\boldsymbol{\theta}_j)}{c_0(\boldsymbol{\theta}_j)} \right)^{2b_j}, \tag{31}$$

where the dependency of J on $\boldsymbol{m}_{\text{eff}}$ (through c_0 and d) is again dropped for brevity, the exponents b_j are chosen as:

$$\begin{cases} b_j = 1 & \text{to minimize the dispersion in direction } \boldsymbol{\theta}_j, \\ b_j = -1 & \text{to maximize the dispersion in direction } \boldsymbol{\theta}_j, \end{cases} \tag{32}$$

and the user-defined weights w_j are used to balance the contribution of each term.

Remark 9. As underlined in [15], due to the scaling of the dispersion terms, trying to only minimize the dispersion without constraints is an ill-posed problem (that results in a refinement of the microstructure at the smallest scale allowed by the discretization). Hereinafter, our primary goal is always to maximize the dispersion in given directions, the "minimization" terms in (31) (for which $b_j = 1$) being added to ensure anisotropic dispersion. Moreover, following Remark 4, we know that d can only admit maxima in orthogonal directions. Therefore, we use at mot $N_\theta = 4$ directions (looking for two maxima and two minima).

From (8) and (9), and using the chain rule, the topological derivatives of c_0 and d are given by:

$$\begin{aligned} \mathcal{D}c_0(\boldsymbol{\theta}) &= \frac{1}{2c_0(\boldsymbol{\theta})} \frac{(\varrho_0 \mathcal{D}\boldsymbol{\mu}_0 - \mathcal{D}\varrho_0 \boldsymbol{\mu}_0) : \boldsymbol{\theta}^{\otimes 2}}{\varrho_0^2} \\ \mathcal{D}d(\boldsymbol{\theta}) &= 2\frac{(\mathcal{D}\boldsymbol{\varrho}_2 \otimes \boldsymbol{\mu}_0 + \boldsymbol{\varrho}_2 \otimes \mathcal{D}\boldsymbol{\mu}_0 - \mathcal{D}\varrho_0 \boldsymbol{\mu}_2 - \varrho_0 \mathcal{D}\boldsymbol{\mu}_2) :: \boldsymbol{\theta}^{\otimes 4}}{\varrho_0^2} - 2\frac{\mathcal{D}\varrho_0}{\varrho_0} d(\boldsymbol{\theta}), \end{aligned} \tag{33}$$

the topological derivative of their ratio is computed as:

$$\mathcal{D}(d/c_0)(\boldsymbol{\theta}) = \frac{c_0(\boldsymbol{\theta}) \mathcal{D}d(\boldsymbol{\theta}) - \mathcal{D}c_0(\boldsymbol{\theta}) d(\boldsymbol{\theta})}{c_0^2(\boldsymbol{\theta})}, \tag{34}$$

and the topological derivative of the cost-functional J defined by (31) is computed using the chain rule.

4.1.1 | Retrieving optimal bilaminates that maximize the dispersion in one direction

Our first examples address the maximization of the dispersion indicator for one direction only *i.e.* $N_\theta = 1$ in (31), in material configurations for which the optimal structures are bilaminates normal to the chosen direction [23], and whose characteristics may be determined analytically from a 1D analysis [23,19].

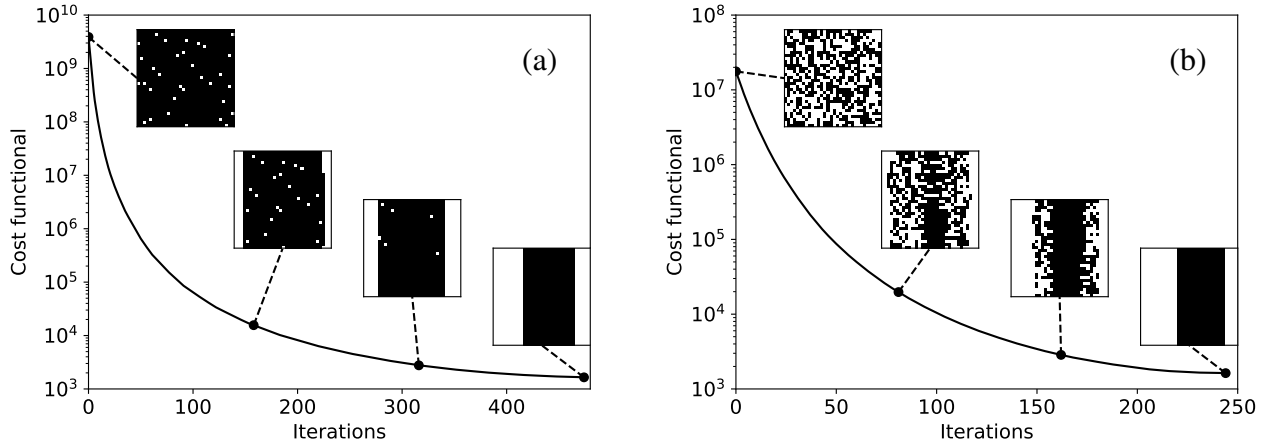

FIGURE 3 Maximization of the dispersion in the horizontal direction, for homogeneous wavespeed. Cost functional values and initial, intermediate and final microstructures discretized on 32×32 grids, obtained using (a) a random unbalanced initalization (32 white pixels) and one-pixel permutations (474 iterations) and (b) a balanced random initialization (as many black than white pixels) and two-pixels exchanges (241 iterations).

Thereafter, we note $\alpha = |Y_A|/|Y|$ the proportion of the first phase, $\gamma_\mu = \mu_B/\mu_A$ the stiffness ratio and $\gamma_\rho = \rho_B/\rho_A$ the density ratio of the two-phase materials. Two configurations of two-phase materials are studied: (i) when the wavespeed is the same in the two phases (*i.e.* $\gamma_\mu = \gamma_\rho$), and (ii) when the density is the same in the two phases (*i.e.* $\gamma_\rho = 1$).

For both configurations, we aim at maximizing the dispersion in the horizontal direction using the cost functional (31) with $N_\theta = 1$, $\boldsymbol{\theta}_1 = \boldsymbol{e}_1$, $w_1 = 1$ and $b_1 = -1$.

Homogeneous wavespeed

This preliminary example is meant to illustrate the speed improvement brought by the level-set-based optimization compared to pixel-by-pixel updates. The contrasts are set to $\gamma_\mu = \gamma_\rho = 2$. The one-pixel permutation and two-pixels exchange algorithms are applied to two random initializations of 32×32 pixels, with respectively 32 and 512 pixels of material A. In both cases, a smooth monotonic decrease of the cost functional is observed, and the expected bilaminate is obtained in resp. 474 and 241 iterations, as plotted in Figure 3. In the other hand, using the level-set algorithm and starting with the same initializations, only few iterations (here, 2 and 3) are needed to reach the same final cells, see Figure 4. In both cases, $\kappa^{(n)} = 1$ for all iterations (the internal loop (d) in step II.3.2 is not activated), *i.e.* the signed topological derivative becomes the new level set at each iteration.

Homogeneous density

When the two phases have the same density, *i.e.* $\rho_A = \rho_B$, optimal bounds of the dispersive coefficient for two-phase materials are known analytically[23]. In particular, the maximal dispersion is obtained for bilaminates, and in this case the homogenized coefficient's expressions are:

$$c_0(\boldsymbol{e}_1) = \sqrt{\frac{\gamma_\mu}{1-\alpha+\alpha\gamma_\mu}}\sqrt{\frac{\mu_A}{\rho_A}}, \qquad d(\boldsymbol{e}_1) = -\frac{\alpha^2(1-\alpha)^2\gamma_\mu(\gamma_\mu-1)^2}{12(1-\alpha+\alpha\gamma_\mu)^3}\frac{\mu_A}{\rho_A}. \tag{35}$$

The optimal proportion $\alpha^{\text{opt}}(\gamma_\mu)$ that maximises the dispersion for a given stiffness contrast γ_μ can therefore be computed as:

$$\alpha^{\text{opt}}(\gamma_\mu) = \arg\max_{\alpha\in[0,1]} \left|\frac{d(\boldsymbol{e}_1)}{c_0(\boldsymbol{e}_1)}\right| = \begin{cases} \dfrac{\sqrt{1+62\gamma_\mu+\gamma_\mu^2}-(7+\gamma_\mu)}{3(\gamma_\mu-1)} & \text{for } \gamma_\mu > 1, \\ 1-\alpha^{\text{opt}}(1/\gamma_\mu) & \text{for } \gamma_\mu < 1. \end{cases} \tag{36}$$

Remark that in the case $\gamma_\mu < 1$, the roles of the two phases is switched compared to the case $\gamma_\mu > 1$. The normalized dispersion indicator $|d/c_0|$ is plotted in Figure 5 versus γ_μ and α, along with the optimal proportion α^{opt}.

To test the efficiency of our optimization algorithm, we attempt to retrieve these results numerically, for several stiffness contrasts. The unit cell is discretized using a 100×100 pixel grid, and initialized with bilaminates with phase ratio $\alpha^{\text{init}} = 0.1$ and

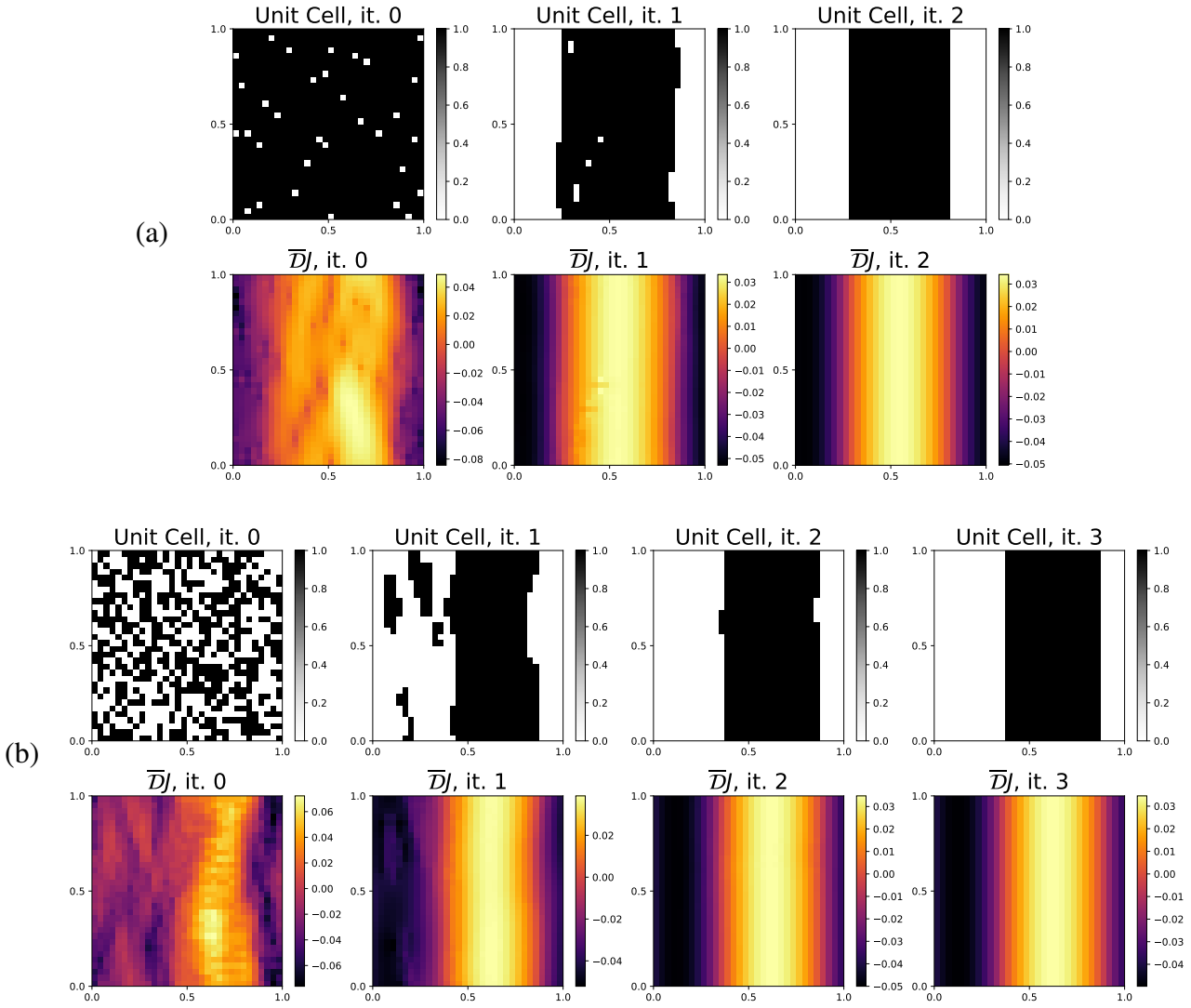

FIGURE 4 Maximization of the dispersion in the horizontal direction, for homogeneous wavespeed. Initial, intermediate and final cells obtained using the level-set algorithm for (a) unbalanced and (b) balanced initial configurations, and corresponding signed topological derivative maps $\boldsymbol{z} \mapsto \overline{DJ}(\boldsymbol{z})$.

$\alpha^{\text{init}} = 0.5$ (*i.e.* some upper and lower bounds of the optimal phase ratio in the considered interval); and with a square inclusion made of material B in a matrix made of material A, with $\alpha^{\text{init}} = 0.5$, as summarized in Table 4. In each tested configuration, the resulting optimal unit cell corresponds indeed to a bilaminate with phase proportion α^{final} close to the theoretical optimal one. It is also seen that using initializations closer to the solution (here, bilaminates) enable to reduce significantly the number of iterations compared to other initializations (here, a squared inclusion). In particular, for one of the computations that used a square as initialization (third line of Table 4), the second part of Algorithm 2 (pixel-by-pixel update) was activated to reach the optimal result.

4.1.2 | Multi-directional optimization

We now apply the optimization algorithm to obtain microstructures that maximize the dispersion in two orthogonal directions. The material contrasts are fixed as $\gamma_\mu = 6$ and $\gamma_\rho = \rho_B/\rho_A = 1.5$.

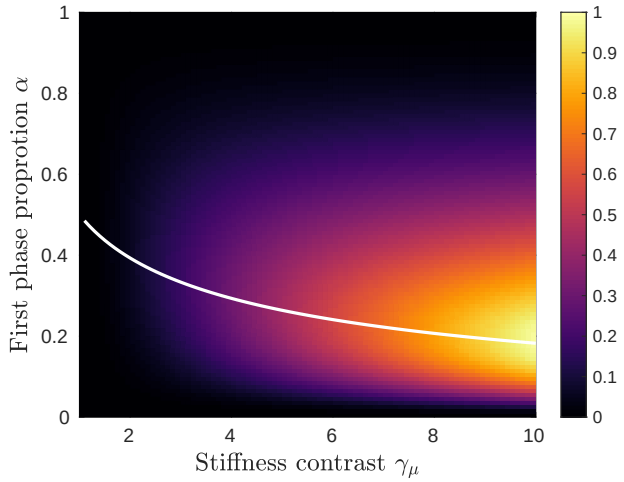

FIGURE 5 Normalized second-order dispersion indicator $|d/c_0|$ for bilaminates in 1D, versus phase proportion $\alpha = |Y_A|/|Y| \in [0, 1]$ and stiffness contrast $\gamma_\mu = \mu_B/\mu_A \in [1, 10]$, and with no density contrast ($\rho_B = \rho_A$). The white curve indicates the optimal phase proportion $\alpha^{\text{opt}}(\gamma_\mu)$ given by (36), that maximises the dispersion for a given contrast γ_μ.

γ_μ	α^{opt}	Initialization	α^{init}	Iterations	α^{final}
2	≈ 0.39	Laminate	0.1	2	0.38
			0.5	3	0.40
		Square	0.5	108 (8+100) ($\star$)	0.39
4	≈ 0.29	Laminate	0.1	2	0.30
			0.5	4	0.30
		Square	0.5	25	0.30
9	≈ 0.19	Laminate	0.1	2	0.20
			0.5	4	0.20
		Square	0.5	22	0.20

TABLE 4 Maximization of the dispersion in the horizontal direction, for homogeneous density ($\rho_B = \rho_A$) and various siffness contrast $\gamma_\mu = \mu_B/\mu_A$. When the second step of Algorithm 2 (pixel-by-pixel optimization) is activated ($\star$), the total number of iterations is decomposed between the two steps.

Maximizing the dispersion in horizontal and vertical directions.

The first example we consider is the maximization of the dispersion indicator $|d/c_0|$ in the horizontal and vertical directions (*i.e.* along the periodicity axis). As it was empirically found to slightly improve the stability of the results, we also minimze the dispersion in the diagonal directions, *i.e.* take $N_\theta = 4$ in (31). The four angles and coefficients (θ_j, w_j, b_j) that define the cost functional (31) are given in Table 5.

Angle θ_j	0	$\pi/4$	$\pi/2$	$3\pi/4$
Weight w_j	1	10	1	10
Exponent b_j	-1	1	-1	1

TABLE 5 Angles and coefficients used for the dispersion maximization in horizontal and vertical directions.

The optimization is performed on a grid of 64×64 pixels, and a number of initial configurations are considered; the corresponding results are summarized in Table 6. In Figure 6 are represented the three initializations leading to the same result,

assumed to the optimal. One can see from the first line (Figure 6(a)) that the optimization procedure slightly improves the dispersive properties of a classical array of circular inclusions, by proposing instead "rounded squares" inclusions. This result can also been obtained by initializing randomly the unit cell, with or without imposing the expecting final 8-fold symmetry (Figure 6(b-c)). We also represented on Figures 7 and 8 the first iterations for these random initializations, along with the signed topological derivative maps.

For completeness, Figure 9 represents initializations leading to sub-optimal results. Curiously, initializing with a squared inclusion (Figure 9 (a)) leads to a qualitatively similar but slightly worse result than the optimal one in terms of the final value of J, as can be seen in Table 6. It is also seen that initializing with another symmetrized random microstructure (Figure 9 (b)) leads to a local minimum featuring a strongly anisotropic coefficient $|d/c_0|$ as desired, but far away from the optimum in terms of the final value of the cost functional J (see Table 6). Finally, initializing with a chessboard-like unit cell (Figure 9 (c)), for which the dispersion is *minimal* in the horizontal and vertical direction, lead to a local minimum corresponding to a nearly-isotropic configuration.

Initialization	Iterations	Final value of J	Final proportion α
Disk	6	5.49×10^2	0.414
Symmetrized random (1)	15 (12+3) ($\star$)	5.49×10^2	0.414
Random	16 (13+3) ($\star$)	5.49×10^2	0.414
Square	7	5.56×10^2	0.432
Symmetrized random (2)	6	8.10×10^2	0.47
Chessboard	48 (5+43) ($\star$)	9.18×10^3	0.36

TABLE 6 Maximization of the dispersion in the horizontal and vertical directions, for six different initializations. When the second step of algorithm 2 (pixel-by-pixel optimization) is activated ($\star$), the total number of iterations is decomposed between the two steps. The first three configurations are represented in Figure 6, and the others in Figure 9.

Maximizing the dispersion in diagonal directions.

As a second example, we maximize the dispersion in the diagonal directions, while minimizing it in the horizontal and vertical direction ($N_\theta = 4$ in (31)). The four angles and coefficients $(\theta_j, \omega_j, b_j)$ that define the cost functional (31) are given in Table 7.

Angle θ_j	0	$\pi/4$	$\pi/2$	$3\pi/4$
Weight ω_j	10	1	10	1
Exponent b_j	1	-1	1	-1

TABLE 7 Angles and coefficients used for the dispersion maximization in diagonal directions.

The same discretization and initializations than in the previous paragraph are used, and the results are summarized in Table 8. Once again, we obtain the same result, assumed to be the optimal one, with three different initialization, as represented in Figure 10. In particular, the chessboard-like initialization is the most efficient to obtain rapidly this optimal result (Figure 10(a)). On the other hand, circular and square inclusions correspond to configurations too far away from the desired properties for the algorithm to reach the optimal result (Figures 12(b-c)). For completeness, the microstructures given by the first iterations from a random initialization (leading to the optimal result), and corresponding signed TD maps are plotted in Figure 11.

As expected, the optimal microstructure corresponds to the rotation of $\pi/4$ and scaling by $\ell \to \ell/\sqrt{2}$ of the microstructure obtained in the previous example (maximization of the dispersion in the vertical and horizontal directions). Indeed, we used the same cost functional, except for the angles, that were rotated by $\pi/4$, but the periodicity axes were unchanged, "forcing" the inclusions to align along the diagonals rather than the horizontal and vertical axes. Accordingly, the maximal dispersion indicator $|d/c_0|$ is divided by 2 (compare the polar plots of Figures 6(a) and 10(a)).

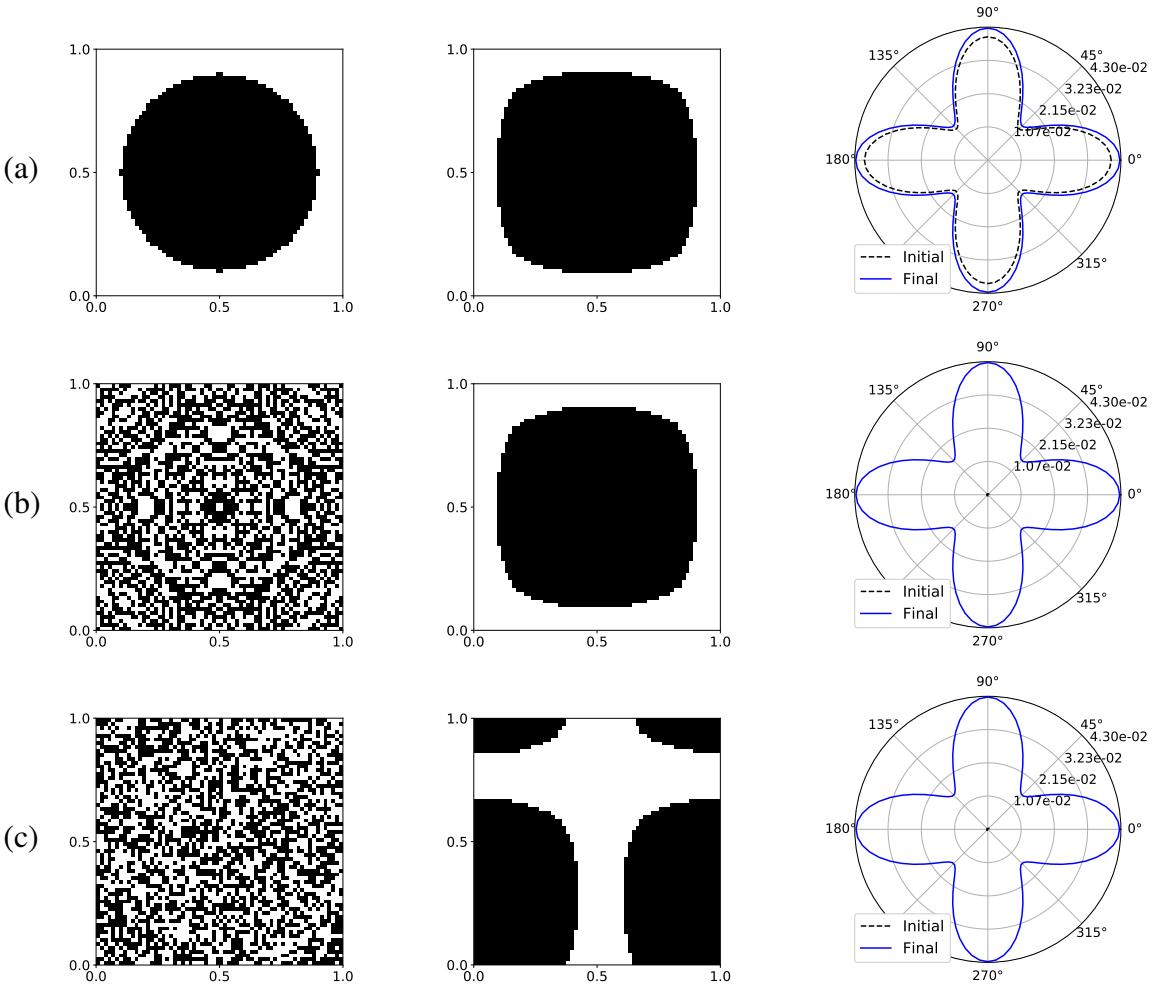

FIGURE 6 Maximization of the dispersion in the horizontal and vertical directions, for three initializations leading to the same result, assumed to be the optimal one: (a) circular inclusion, (b) symmetrized random distribution of materials, and (c) completely random distribution of material. From left to right: initial and final unit cells, and polar plot of the dispersion indicator $|d/c_0|$ for these two cells.

Initialization	Iterations	Final value of J	Final proportion α
Chessboard	5	2.2×10^3	0.42
Symmetrized random (1)	7	2.2×10^3	0.42
Random	11	2.2×10^3	0.42
Symmetrized random (2)	222 (31+191) ($\star$)	2.51×10^3	0.41
Square	18 (6+12) ($\star$)	2.33×10^3	0.39
Disk	118 (5+113) ($\star$)	2.4×10^3	0.36

TABLE 8 Maximisation of dispersion in diagonal directions, for six initializations. When the second step of algorithm 2 (pixel-by-pixel optimization) is activated ($\star$), the total number of iterations is decomposed between the two steps. The first three configurations are represented in Figure 10, and the others in Figure 12.

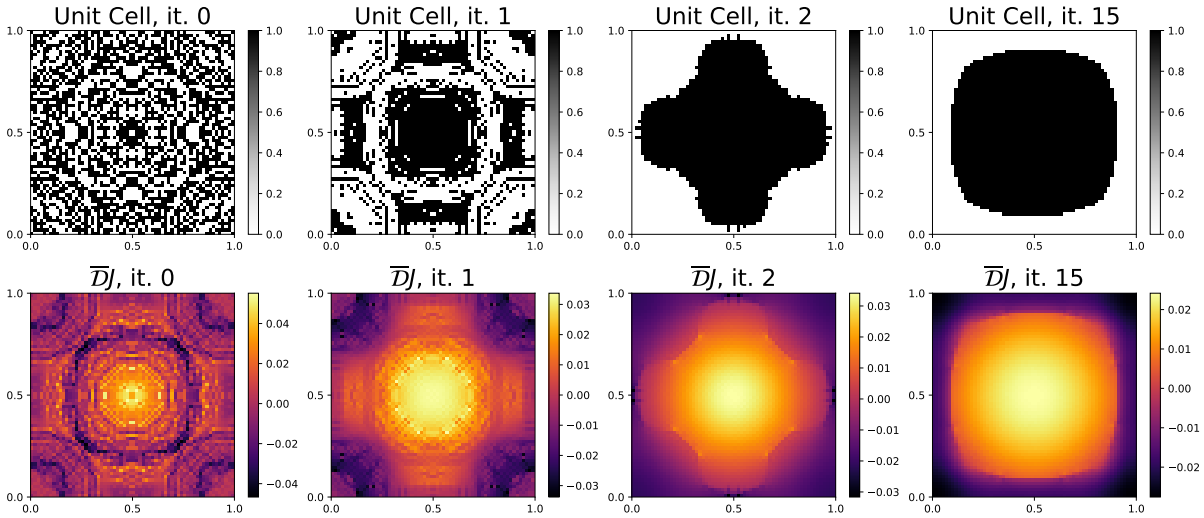

FIGURE 7 Maximization of the dispersion in the horizontal and vertical directions: iterations of the microstructure and signed topological derivative maps, for a symmetrical random initialization (Figure 6(b)).

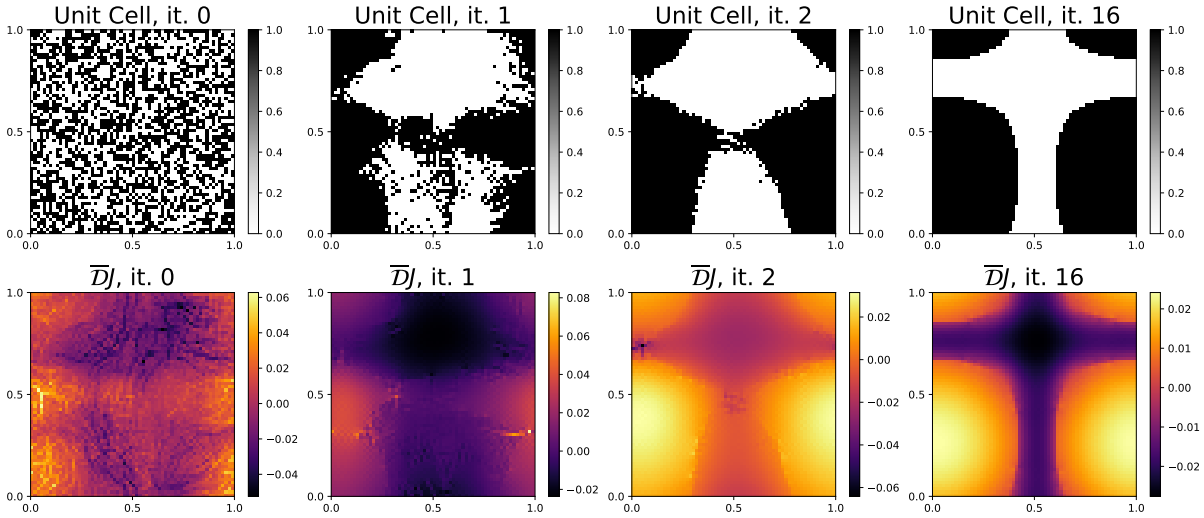

FIGURE 8 Maximization of the dispersion in the horizontal and vertical directions: iterations of the microstructure and signed topological derivative maps, for a completely random initialization (Figure 6(c)).

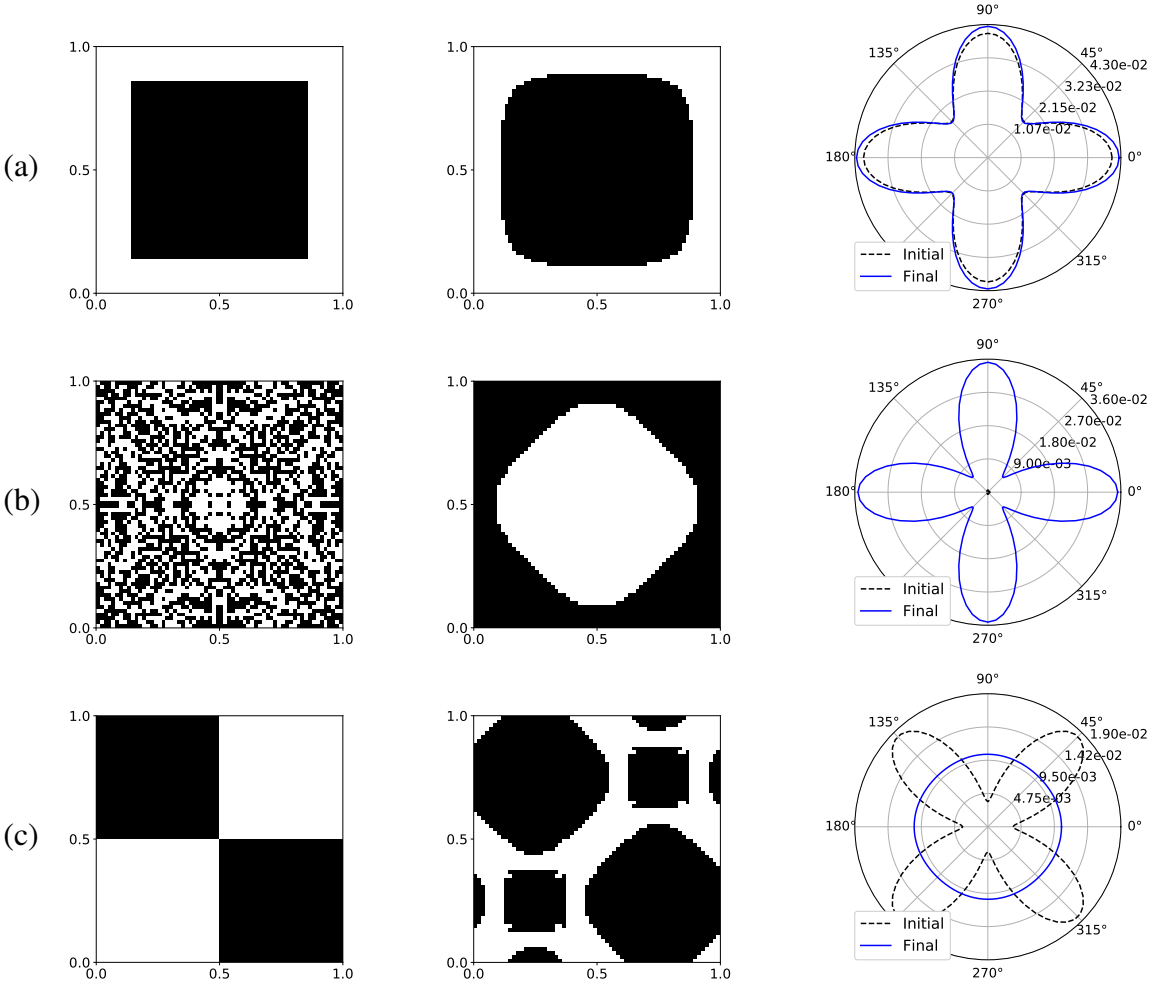

FIGURE 9 Maximization of the dispersion in the horizontal and vertical directions, for three initializations leading to sub-optimal results: (a) square inclusion, (b) symmetrized random distribution of materials, and (c) chessboard-like unit cell. From left to right: initial and final unit cells, and polar plot of the dispersion indicator $|d/c_0|$ for these two cells.

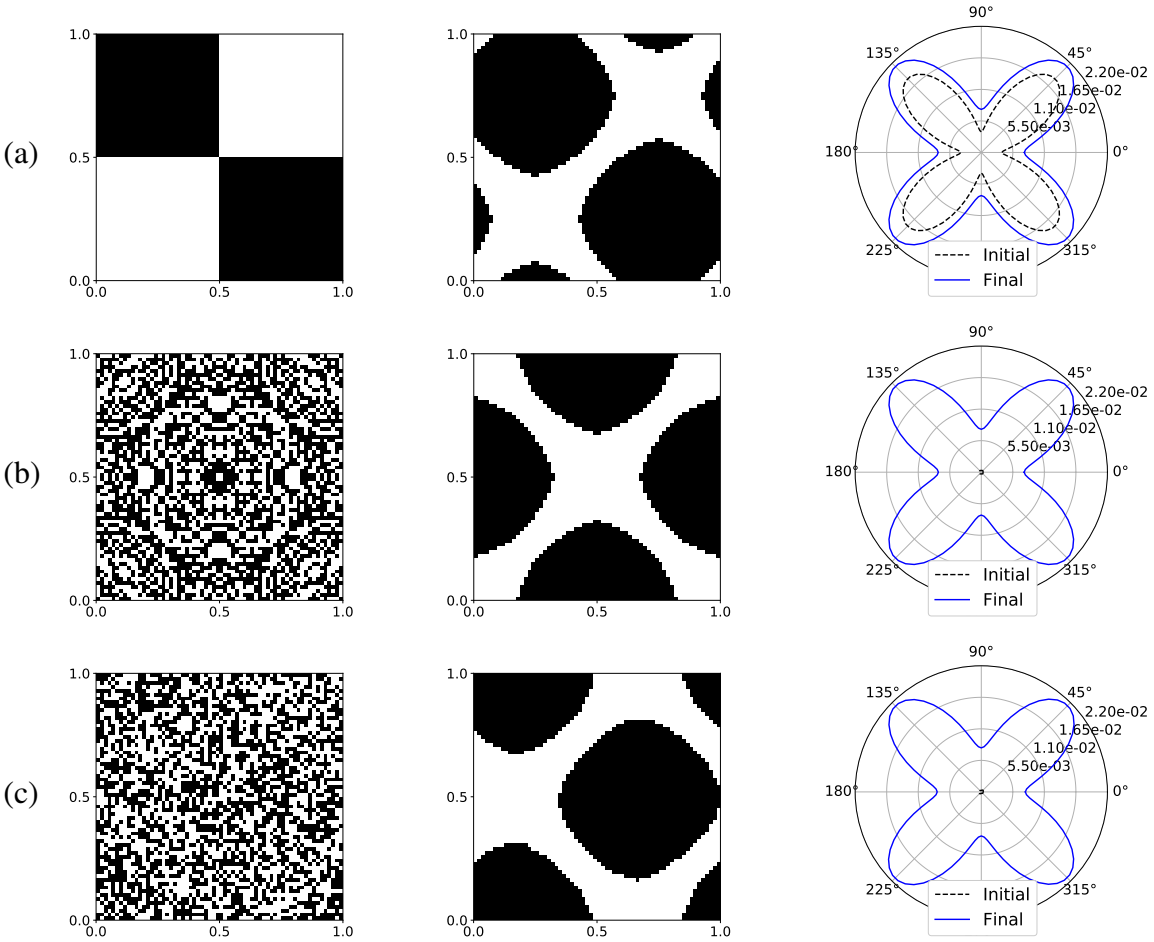

FIGURE 10 Maximisation of dispersion in diagonal directions, for three initializations leading to the same value of the cost functional, assumed to be the optimal one: (a) chessboard-like unit cell, (b) symmetrized random distribution of materials, and (c) completely random distribution of materials. From left to right: initial and final unit cells, and polar plot of the dispersion indicator $|d/c_0|$ for these two cells.

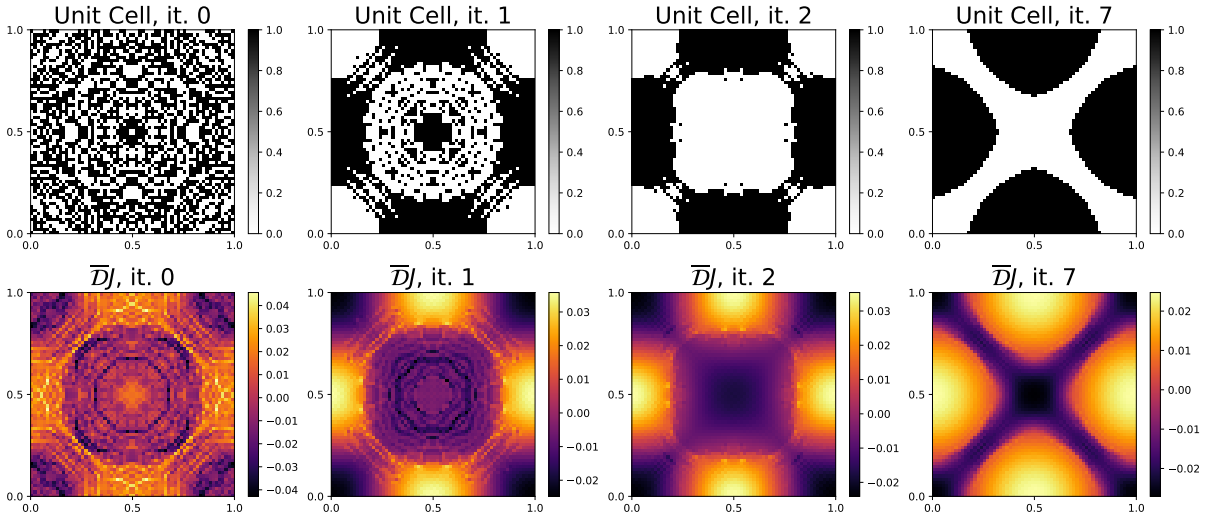

FIGURE 11 Maximisation of dispersion in diagonal directions: iterations of the microstructure and signed topological derivative maps, for the symmetrical random initialization (Figure 10(b)).

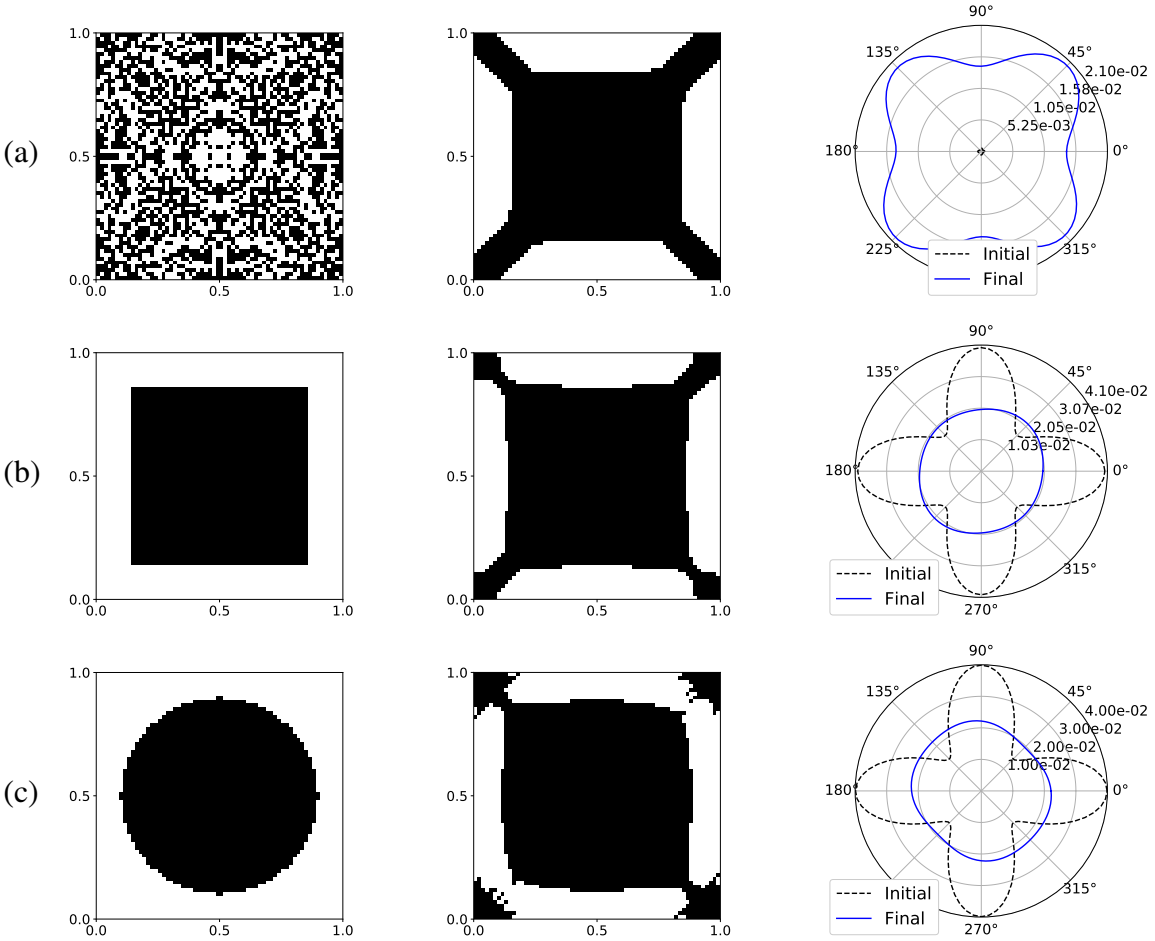

FIGURE 12 Maximisation of dispersion in diagonal directions, for three initializations leading to sub-optimal results: (a) symmetrized random distribution of materials, (b) square inclusion, and (c) circular inclusion. From left to right: initial and final unit cells, and polar plot of the dispersion indicator $|d/c_0|$ for these two cells.

4.1.3 | Bloch-Floquet analysis of the designed microstructure

To complete the results of this section, we analyse in more details the structure obtained while maximizing the dispersion in horizontal and vertical directions, see Figure 6. To facilitate this analysis, the boundary of the "rounded-corners square" inclusion obtained on a 64×64 pixel grid is first fitted by a quartic curve with equation:

$$y_1^4 + y_2^4 + \frac{y_1^2 y_2^2}{4} - R^4 = 0, \quad \text{with } R = 0.405, \tag{37}$$

as plotted in Figure 13. This approximated model is then used to perform a computation of the dispersion curves given by the Floquet-Bloch eigenfrequencies of the unit cell when the wavevector $\boldsymbol{k}$ spans the edges of the reduced Brillouin zone, see Figure 14. To do so, we adapted the routines provided on Vincent Laude's webpage[1] as supplementary material of his monograph[1], implemented in the finite element platform FREEFEM++[44]. For comparison purposes, we also computed the dispersion curves associated to the "almost optimal" disk used as initialization, see Figure 6(a).

From the results in Figure 14, one can see that the anisotropic dispersive properties of the considered cells extend beyond the low-frequency regime covered by the homogenized model, as the onset of the first band-gap appears at higher frequencies for $\theta = \pi/4$ (section Γ-M) than for $\theta = 0$ (section Γ-X). Moreover, as expected from the polar plot of $|d/c_0|$ in Figure 6(a), the acoustic branches, corresponding to the first Bloch mode, are nearly superimposed for the two cells. The optimization process, acting on the slope c_0 and third derivative (proportional to d/c_0) of the curves $k \mapsto \omega(k, \boldsymbol{\theta})$ at origin $k = 0$, seems to have mainly increased slightly the limit velocity c_0 by "converting" the circular inclusion to the quartic inclusion. On the contrary, the discrepancy between the first optical branches, corresponding to the second Bloch mode, is much larger. This strong sensitivity of dispersive effects to moderate topology changes, at higher frequencies, is a strong motivation to combine our methodology with models that describe the wave motion at these frequencies[16,18], in a future work.

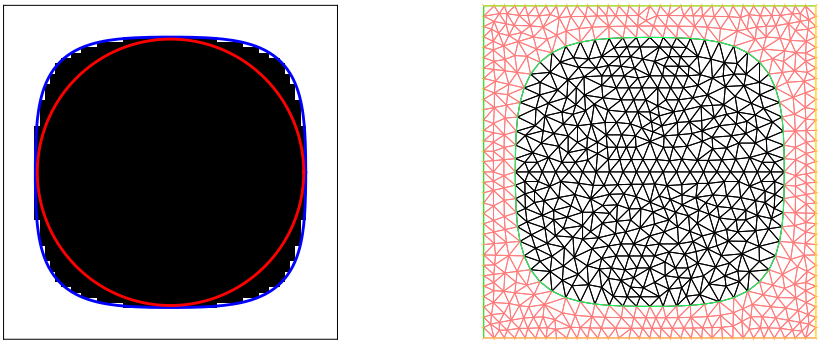

FIGURE 13 Left: optimized cell on a 64×64 pixel grid, fitting quartic curve (37) (blue), and boundary of the disk used as initialization (red). Right: mesh of the cell and quartic inclusion used in the Floquet-Bloch computations.

[1] http://members.femto-st.fr/vincent-laude/freefem-scripts-numerical-simulation-phononic-crystals

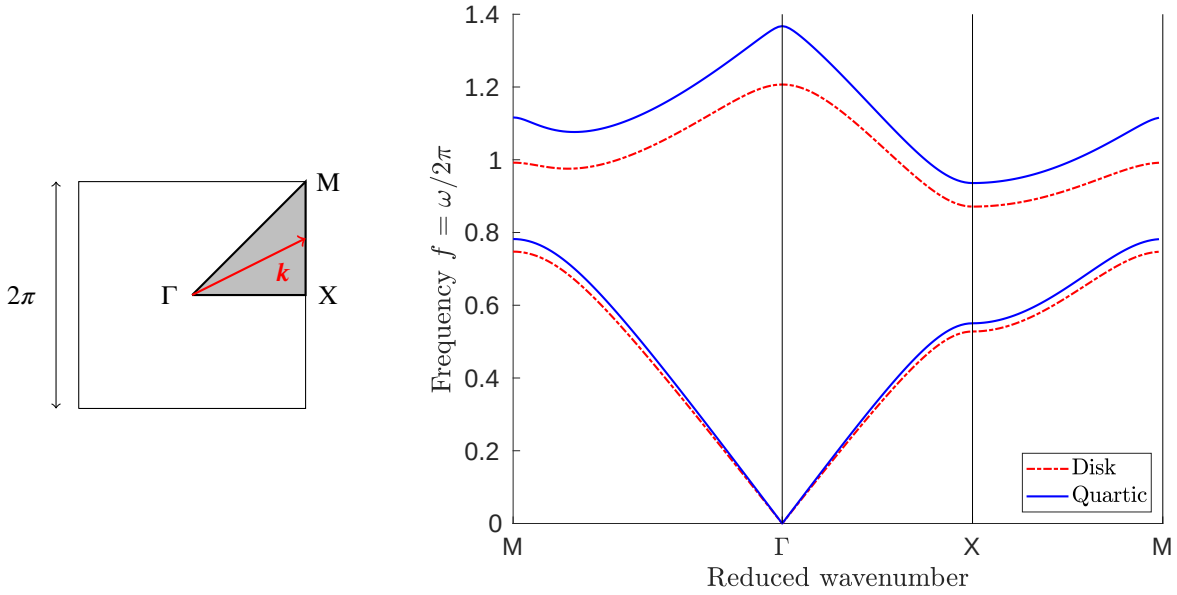

FIGURE 14 Left: reciprocal unit cell, and reduced Brillouin zone (grey triangle). Right: acoustic and first optical branches (corresponding to the first and second Floquet-Bloch eigenfrequencies), for the circular inclusion (red) and the quartic approximation of the optimal inclusion (blue), see Figure 13. The reduced wavevector's tip follows the edges of the reduced Brillouin zone.

4.2 | Reconstructing a microstructure from phase velocity data

As a last example, we apply the optimization algorithm to an identification problem already partially addressed in [27]: we aim at reconstructing an unknown microstructure from measurements of its effective dynamical properties. More precisely, we suppose that the collected measurements are the phase velocities $c^{\text{obs}}(k_p, \boldsymbol{\theta}_j)$ for various wavenumbers k_p, $p = 1, \dots, N_k$ and in various directions of propagation $\boldsymbol{\theta}_j = (\cos\theta_j, \sin\theta_j)$, $j = 1, \dots, N_\theta$. These data are to be compared to the phase velocity $c(k, \boldsymbol{\theta}) = \omega(k, \boldsymbol{\theta})/k$ obtained by second-order homogenization of the trial periodic structures, *i.e.* with $\omega(k, \boldsymbol{\theta})$ given by (6).

Cost functional and topological derivative

We first define the classical least-square cost functional J_c evaluating the misfit between measured and homogenized velocities, for a given couple of wavenumber and direction $(k, \boldsymbol{\theta})$:

$$J_c(k, \boldsymbol{\theta}) = \frac{1}{2}\left[c(k, \boldsymbol{\theta}) - c^{\text{obs}}(k, \boldsymbol{\theta})\right]^2, \tag{38}$$

The dependency of J_c on the effective properties $\boldsymbol{m}_{\text{eff}}$, dropped for simplicity, is embedded in the definition of c. We also define the dynamic cost functional $J_{\Delta c}$, extracting the effects of dispersion, as

$$J_{\Delta c}(k, \boldsymbol{\theta}) = \frac{1}{2}\left[\Delta c(k, \boldsymbol{\theta}) - \Delta c^{\text{obs}}(k, \boldsymbol{\theta})\right]^2, \qquad \Delta c(k, \boldsymbol{\theta}) = c(k, \boldsymbol{\theta}) - c(k_{\min}, \boldsymbol{\theta}), \tag{39}$$

where $k_{\min}$ is the smallest wavenumber for which measurements are available; we assume that $k_{\min}\ell \ll 1$ so that $c(k_{\min}, \boldsymbol{\theta})$ is close to the low-frequency limit phase velocity $c_0(\boldsymbol{\theta})$. The topological sensitivities of these two misfit functionals are:

$$\begin{aligned} \mathcal{D}J_c(k, \boldsymbol{\theta}; \boldsymbol{z}) &= \left[c(k, \boldsymbol{\theta}) - c^{\text{obs}}(k, \boldsymbol{\theta})\right] \mathcal{D}c(k, \boldsymbol{\theta}; \boldsymbol{z}), \\ \mathcal{D}J_{\Delta c}(k, \boldsymbol{\theta}; \boldsymbol{z}) &= \left[\Delta c(k, \boldsymbol{\theta}) - \Delta c^{\text{obs}}(k, \boldsymbol{\theta})\right] \Big(\mathcal{D}c(k, \boldsymbol{\theta}; \boldsymbol{z}) - \mathcal{D}c(k_{\min}, \boldsymbol{\theta}; \boldsymbol{z})\Big), \end{aligned} \tag{40}$$

where the topological derivative $\mathcal{D}c$ of the phase velocity is:

$$\mathcal{D}c(k, \boldsymbol{\theta}; \boldsymbol{z}) = \frac{\left[\mathcal{D}\boldsymbol{\mu}_0 : \boldsymbol{\theta}^{\otimes 2} - \ell^2 k^2 \mathcal{D}\boldsymbol{\mu}_2 :: \boldsymbol{\theta}^{\otimes 4} - (c(k, \boldsymbol{\theta}))^2 \left(\mathcal{D}\rho_0 - \ell^2 k^2 \mathcal{D}\boldsymbol{\rho}_2 : \boldsymbol{\theta}^{\otimes 2}\right)\right](\boldsymbol{z})}{2\left(\rho_0 - \ell^2 k^2 \boldsymbol{\rho}_2 : \boldsymbol{\theta}^{\otimes 2}\right)}. \tag{41}$$

In this setting, we finally define the aggregate cost functionals as

$$J_c^{\text{tot}} = \sum_{j=1}^{N_\theta} J_c(k_{\min}, \boldsymbol{\theta}_j) \qquad \text{and} \qquad J_{\Delta c}^{\text{tot}} = \sum_{j=1}^{N_\theta} \sum_{p=1}^{N_k} J_{\Delta c}(k_p, \boldsymbol{\theta}_j), \tag{42}$$

that measure respectively the misfits of quasitatic velocities and dispersion for all measurements, and whose sensitivities $\mathcal{D}J_c^{\text{tot}}$ and $\mathcal{D}J_{\Delta c}^{\text{tot}}$ are computed by way of (40-41).

In [27], these sensitivities were computed once on a reference chessboard-like unit cell, to localize a damaged quarter-cell in the unit cell of a defective material. It was observed that J_c^{tot} was useful to determine the nature of the defect (softer or stiffer) but had no localization capabilities, whereas $J_{\Delta c}^{\text{tot}}$ was able to distinguish between intact and defective quarter-cells, *i.e.* was more sensitive to geometric alterations. In order to apply the optimization algorithm 1 to *reconstruct* a given unit cell from similar data, we employ a weighted combination of the two cost functionals above:

$$J^w = wJ_c^{\text{tot}} + J_{\Delta c}^{\text{tot}}. \tag{43}$$

Data and constraints

To avoid the so-called *inverse crime*, we use values of c^{obs} resulting from Floquet-Bloch analysis (instead of homogenization) of a two-phases chessboard-like unit cell, whose material ratios are $\mu_B/\mu_A = 7$ and $\rho_B/\rho_A = 1.2$ (as already done in [27]). The plane-wave probing grid has $N_\theta = 7$ incident directions with $\theta_j = (j-3)\pi/8$, $j = 1, \dots, N_\theta$, and $N_k = 10$ wavenumbers $k_p = 2p\pi/30$, $p = 1, \dots, N_k$. With such hypotheses, the shortest wavelength used to probe the periodic structure is $\lambda_{\min} = 2\pi/k_{N_k} = 3 = 3\ell$ (since we work on the unit cell data without normalization, $\ell = 1$).

To facilitate the computation, the following constraints are set in the optimization algorithm:

- The phase properties are set identical to those of the chessboard ($\mu_B/\mu_A = 7$ and $\rho_B/\rho_A = 1.2$).
- The volume fraction of each phase is constrained: $|Y_A| = |Y_B| = 1/2$ as in the chessboard. In practice, this is done by rescaling the level-set at each iteration.

In other words, the only missing information to reconstruct the chessboard cell is the *geometrical distribution* of the phases into the cell.

Results

The weighting parameter w is fixed to three different values: $w \in \{0, 0.1, 0.2\}$. Using the completely random initialization displayed in Figures 6(c) and 10(c), we obtain the results displayed in Figure 15. For $w = 0$, *i.e.* when taking only the dipersion data into account, a very good agreement is observed between the (homogenized) dispersion of the obtained structure and the (Floquet-Bloch) target dispersion, whereas the limit velocities differ. As expected, a better fit of the limit velocity c_0 is then obtained for larger values of the weighting parameter w, but at the price of a larger misfit with the dispersion measurements $\Delta c(k_p, \boldsymbol{\theta}_j)$, and more "blurred" interfaces between the two material phases. In all cases, a chessboard-like structure is recovered, illustrating the capabilities of the algorithm to recover –at least qualitatively– the microstructural distribution of a periodic material from macroscopic data.

5 | SUMMARY AND PERSPECTIVES

In this work, we presented a topological optimization procedure, relying on robust and simply implemented analytical and numerical tools: second-order asymptotic homogenization, topological derivatives, FFT-accelerated cell problem solver. Examples assert the capabilities of this procedure to (i) recover known analytical results on optimal bilaminates for unidimensional wave propagation, (ii) provide optimal microstructures that realize an objective anisotropic effective dispersion, and (iii) identify microstructures from effective phase velocity data. The effects of varying the initalizations (which can enable a faster convergence towards a better optimum of the cost functional) and changing the relative weights of the quasistatic and dispersive data were qualitatively studied. Moreover, this study sets a framework that can easily be extended to other geometrical and physical configurations or objectives.

First of these extensions, a work in progress concerns the application of the optimization algorithm to *rows* of inclusions that span only a strip in the plane, and whose homogenization results in equivalent transmission condition rather than an enrichement of the wave equation[45]; the optimization process will aim at tuning these transmission conditions to obtain various anisotropic effects, *e.g.* incidence direction-dependent transmission or reflection coefficients. The extension to in-plane and 3D elasticity is then envisaged, using the second-order homogenization results existing for elastic composites[46], that lead to the so-called strain gradient models[29,22]. Leaning on the much richer physics of elastic waves captured by these models, one could design structures combining exotic static properties (*e.g.* auxetic structures[13]) with wave-related properties such as mode conversion and dispersion. We also aim at extending the procedure to *resonant metamaterials*, see *e.g.*[6] for bulk homogenization and[47] for resonant interfaces. Finally, it is worth mentioning that the present work paves the way towards an extension to higher-frequency homogenization regimes. Indeed, building on the high-frequency homogenization framework introduced by[17], the *second-order* asymptotic framework employed here is also able to describe the effective behavior of periodic materials about the apexes of the Brillouin zone[18]. Computing the latter would necessitate the development of a FFT-based and matrix-free Bloch-Floquet solver in order to build a consistent extension of our methodology. This would also lead to an extension of recent topological optimization works[16] that use *leading-order* high-frequency homogenization.

Another improvement direction, that should be combined with the propositions above, concerns the efficiency of the numerical components of the procedure. A first idea is to develop a "pixel sensitivity" that could replace the topological sensitivity to better account for the chosen discretization of the unit cell, *i.e.* to consider the sensitivity to a pixel change at the discrete level rather than to an infinitesimal phase change at the continuous level, similarly to the discrete shape sensitivity used in[15] instead of the formula derived from continuous analysis. Then, the optimization algorithm could be modified to handle *multi-phase* materials following the recent proposal of[48]. Finally, the "basic scheme" of the FFT-accelerated method initially proposed in[28], that we used for simplicity, could be replaced by one of the many refined methods that were developed since then, see *e.g.*[38,49] and the references therein, especially to deal with more expansive cell problems stemming from the elasticity system.

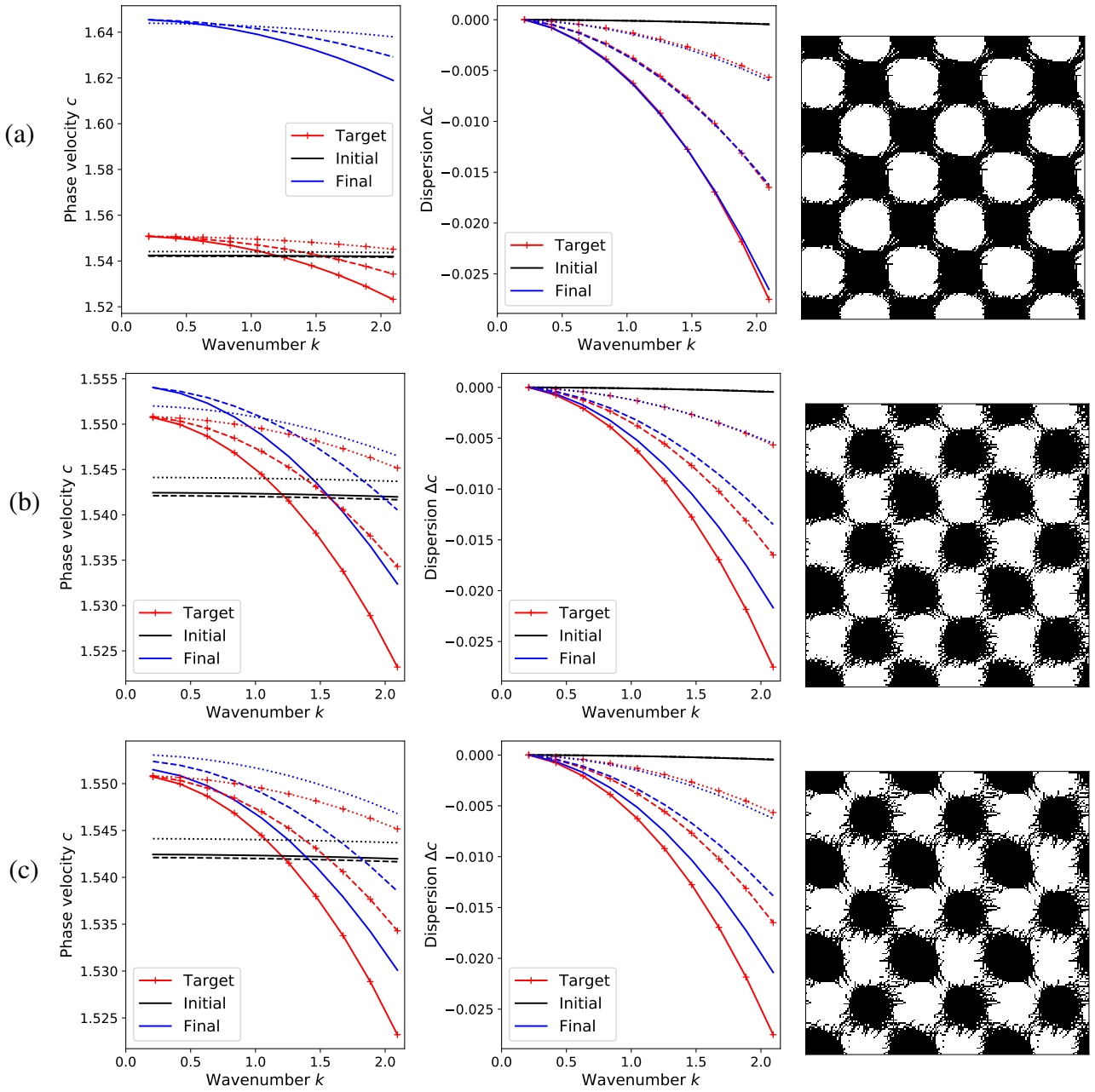

FIGURE 15 Result of the chessboard recovering process for (a) $w = 0$ (*i.e.* $\boldsymbol{J}^w = \boldsymbol{J}^{\text{tot}}_{\Delta c}$), (b) $w = 0.1$, and (c) $w = 0.2$. From left to right: (i) initial, target and final phases velocities, in three directions: $\theta = 0$ (dotted), $\theta = \pi/8$ (dashed) and $\theta = \pi/4$ (solid); (ii) initial, target and final dispersions, in the same directions; and (iii) final microstructures (3×3 unit cells).

ACKNOWLEDGEMENTS

The project leading to this publication has received funding from Excellence Initiative of Aix-Marseille University - A*MIDEX, a French “Investissements d’Avenir” program. It has been carried out in the framework of the Labex MEC. The authors thank Bruno Lombard for fruitful discussions, and acknowledge the stimulating exchanges promoted by the GDR MecaWave.

APPENDIX

A MATHEMATICAL DEFINITIONS

A.1 Tensorial notations

In equations such as (2) the gradient operator $\boldsymbol{\nabla}$ and its powers, which satisfy $\boldsymbol{\nabla}^p = \boldsymbol{\nabla}(\boldsymbol{\nabla}^{p-1})$, and the divergence operator are defined for any tensor field $\boldsymbol{T}(\boldsymbol{x})$ as

$$\boldsymbol{\nabla}\boldsymbol{T}(\boldsymbol{x}) = \boldsymbol{e}_i \otimes \frac{\partial}{\partial z_i}\boldsymbol{T}(\boldsymbol{x}) \qquad \text{and} \qquad \operatorname{div}\boldsymbol{T}(\boldsymbol{x}) = \boldsymbol{e}_i \cdot \frac{\partial}{\partial x_i}\boldsymbol{T}(\boldsymbol{x})$$

where $(\boldsymbol{e}_i)_i$ denotes the canonical basis in $\mathbb{R}^2$.

The notations $\cdot^{\mathrm{psym}}$ and $\cdot^{\mathrm{sym}}$ denote respectively partial symmetrization on all indices except the first one and complete symmetrization by permutation of all the indices, *e.g.* for any third-order tensor $\boldsymbol{T} = (T_{ijk})$ it holds

$$(\boldsymbol{T}^{\mathrm{psym}})_{ijk} = \frac{1}{2}\left(T_{ijk} + T_{ikj}\right) \qquad \text{and} \qquad (\boldsymbol{T}^{\mathrm{sym}})_{ijk} = \frac{1}{6}\left(T_{ijk} + T_{ikj} + T_{jik} + T_{jki} + T_{kij} + T_{kji}\right).$$

Moreover, the term $\boldsymbol{T}^{\otimes p}$ denotes p-th power of $\boldsymbol{T}$ owing to the standard tensorial product, *e.g.*

$$\boldsymbol{T}^{\otimes 2} = \boldsymbol{T} \otimes \boldsymbol{T} \quad \text{and} \quad \boldsymbol{T}^{\otimes 4} = \boldsymbol{T} \otimes \boldsymbol{T} \otimes \boldsymbol{T} \otimes \boldsymbol{T}.$$

A.2 Periodic fields and Fourier transforms

Consider a unit-cell Y allowing to fill the space $\mathbb{R}^2$ by translation along the vectors $\boldsymbol{Y}_1, \boldsymbol{Y}_2$. The lattice $\mathcal{R}$ generated by these vectors is defined as

$$\mathcal{R} = \left\{\boldsymbol{Y},\ \boldsymbol{Y} = n_1\boldsymbol{Y}_1 + n_2\boldsymbol{Y}_2,\ n_j \in \mathbb{Z}\right\}.$$

Define spaces of periodic scalar functions as:

$$L^2_{\mathrm{per}}(Y) = \left\{f \in L^2_{\mathrm{loc}}(\mathbb{R}^2),\ f(\boldsymbol{y}+\boldsymbol{Y}) = f(\boldsymbol{y}),\ \text{a.e. } \boldsymbol{y} \in \mathbb{R}^2,\ \forall \boldsymbol{Y} \in \mathcal{R}\right\},$$
$$H^1_{\mathrm{per}}(Y) = \left\{f \in H^1_{\mathrm{loc}}(\mathbb{R}^2),\ f \in L^2_{\mathrm{per}}(Y),\ \partial_{y_j} f \in L^2_{\mathrm{per}}(Y),\ j = 1,2\right\}.$$

Likewise, we denote as $\boldsymbol{L}^2_{\mathrm{per}}(Y)$ the space of periodic tensors fields (of any order) whose components are functions belonging to $L^2_{\mathrm{per}}(Y)$.

The Fourier transform $\hat{f}$ of f is defined as:

$$\hat{f}(\boldsymbol{\xi}) = \mathscr{F}[f](\boldsymbol{\xi}) = \frac{1}{|Y|}\int_Y f(\boldsymbol{y}) e^{-\mathrm{i}\boldsymbol{\xi}\cdot\boldsymbol{y}}\,\mathrm{d}\boldsymbol{y}, \quad \text{where} \quad \mathrm{i} = \sqrt{-1}.$$

Let $\mathcal{R}^*$ denote the reciprocal lattice of $\mathcal{R}$ generated by the vectors

$$\boldsymbol{Y}_1^* = -\frac{2\pi}{|Y|}\boldsymbol{R}\boldsymbol{Y}_2 \qquad \text{and} \qquad \boldsymbol{Y}_2^* = \frac{2\pi}{|Y|}\boldsymbol{R}\boldsymbol{Y}_1$$

where $\boldsymbol{R}$ is the $\pi/2$ rotation matrix. Then, according to Plancherel's theorem:

$$\frac{1}{|Y|}\int_Y \left|f(\boldsymbol{y})\right|^2 d\boldsymbol{y} = \sum_{\boldsymbol{\xi}\in\mathcal{R}^*}\left|\hat{f}(\boldsymbol{\xi})\right|^2,$$

and therefore

$$f \in L^2_{\mathrm{per}}(Y) \quad \Leftrightarrow \quad \sum_{\boldsymbol{\xi}\in\mathcal{R}^*}\left|\hat{f}(\boldsymbol{\xi})\right|^2 < +\infty.$$

The original periodic function f in $L^2_{\mathrm{per}}(Y)$ can be reconstructed from its Fourier transform by

$$f(\boldsymbol{y}) = \mathscr{F}^{-1}[f](\boldsymbol{y}) = \sum_{\boldsymbol{\xi}\in\mathcal{R}^*}\hat{f}(\boldsymbol{\xi})e^{\mathrm{i}\boldsymbol{\xi}\cdot\boldsymbol{y}}.$$

References

1. Laude V. *Phononic crystals*. De Gruyter . 2015

2. Hussein MI, Leamy MJ, Ruzzene M. Dynamics of Phononic Materials and Structures: Historical Origins, Recent Progress, and Future Outlook. *Applied Mechanics Reviews* 2014; 66(4): 040802. doi: 10.1115/1.4026911

3. Srivastava A. Elastic metamaterials and dynamic homogenization: a review. *International Journal of Smart and Nano Materials* 2015; 6(1): 41–60. doi: 10.1080/19475411.2015.1017779

4. Krushynska A, Kouznetsova V, Geers M. Towards optimal design of locally resonant acoustic metamaterials. *Journal of the Mechanics and Physics of Solids* 2014; 71: 179–196. doi: 10.1016/j.jmps.2014.07.004

5. Palermo A, Krödel S, Marzani A, Daraio C. Engineered metabarrier as shield from seismic surface waves. *Scientific Reports* 2016; 6(1). doi: 10.1038/srep39356

6. Vondřejc J, Rohan E, Heczko J. Shape optimization of phononic band gap structures using the homogenization approach. *International Journal of Solids and Structures* 2017; 113-114: 147 - 168. doi: https://doi.org/10.1016/j.ijsolstr.2017.01.038

7. Schwan L, Umnova O, Boutin C. Sound absorption and reflection from a resonant metasurface: Homogenisation model with experimental validation. *Wave Motion* 2017; 72: 154–172. doi: 10.1016/j.wavemoti.2017.02.004

8. He J, Kang Z. Achieving directional propagation of elastic waves via topology optimization. *Ultrasonics* 2018; 82: 1 - 10. doi: https://doi.org/10.1016/j.ultras.2017.07.006

9. Kook J, Jensen JS. Topology optimization of periodic microstructures for enhanced loss factor using acoustic-structure interaction. *International Journal of Solids and Structures* 2017: -. doi: https://doi.org/10.1016/j.ijsolstr.2017.06.001

10. Bensoussan A, Lions JL, Papanicolau G. *Asymptotic Analysis for Periodic Structures*. Amsterdam: North-Holland . 1978.

11. Milton GW. *The Theory of Composites*. Cambridge university press . 2002.

12. Giusti SM, Novotny AA, Souza Neto dEA. Sensitivity of the macroscopic response of elastic microstructures to the insertion of inclusions. *Proceedings of the Royal Society of London A: Mathematical, Physical and Engineering Sciences* 2010. doi: 10.1098/rspa.2009.0499

13. Amstutz S, Giusti SM, Novotny AA, Souza Neto dEA. Topological derivative for multi-scale linear elasticity models applied to the synthesis of microstructures. *International Journal for Numerical Methods in Engineering* 2010; 84(6): 733–756. doi: 10.1002/nme.2922

14. Oliver J, Ferrer A, Cante JC, Giusti SM, Lloberas-Valls O. *On Multi-scale Computational Design of Structural Materials Using the Topological Derivative*: 289–308; Cham: Springer International Publishing . 2018

15. Allaire G, Yamada T. Optimization of dispersive coefficients in the homogenization of the wave equation in periodic structures. *Numerische Mathematik* 2018; 140(2): 265–326. doi: 10.1007/s00211-018-0972-4

16. Noguchi Y, Yamada T, Izui K, Nishiwaki S. Topology optimization for hyperbolic acoustic metamaterials using a high-frequency homogenization method. *Computer Methods in Applied Mechanics and Engineering* 2018; 335: 419–471. doi: 10.1016/j.cma.2018.02.031

17. Craster RV, Kaplunov J, Pichugin AV. High-frequency homogenization for periodic media. *Proceedings of the Royal Society of London A: Mathematical, Physical and Engineering Sciences* 2010; 466(2120): 2341–2362. doi: 10.1098/rspa.2009.0612

18. Guzina BB, Meng S, Oudghiri-Idrissi O. A rational framework for dynamic homogenization at finite wavelengths and frequencies. *Proceedings of the Royal Society A: Mathematical, Physical and Engineering Sciences* 2019; 475(2223): 20180547. doi: 10.1098/rspa.2018.0547

19. Wautier A, Guzina BB. On the second-order homogenization of wave motion in periodic media and the sound of a chessboard. *Journal of the Mechanics and Physics of Solids* 2015; 78: 382 - 414. doi: https://doi.org/10.1016/j.jmps.2015.03.001

20. Allaire G, Briane M, Vanninathan M. A comparison between two-scale asymptotic expansions and Bloch wave expansions for the homogenization of periodic structures. *SeMA Journal* 2016; 73(3): 237–259. doi: 10.1007/s40324-016-0067-z

21. Askes H, Aifantis EC. Gradient elasticity in statics and dynamics: An overview of formulations, length scale identification procedures, finite element implementations and new results. *International Journal of Solids and Structures* 2011; 48(13): 1962–1990. doi: 10.1016/j.ijsolstr.2011.03.006

22. Auffray N, Dirrenberger J, Rosi G. A complete description of bi-dimensional anisotropic strain-gradient elasticity. *International Journal of Solids and Structures* 2015; 69–70: 195–206. doi: 10.1016/j.ijsolstr.2015.04.036

23. Conca C, Martín JS, Smaranda L, Vanninathan M. Optimal bounds on dispersion coefficient in one-dimensional periodic media. *Mathematical Models and Methods in Applied Sciences* 2009; 19(09): 1743–1764. doi: 10.1142/s0218202509003930

24. Bălilescu L, Conca C, Ghosh T, Martín JS, Vanninathan M. The Dispersion Tensor and Its Unique Minimizer in Hashin–Shtrikman Micro-structures. *Archive for Rational Mechanics and Analysis* 2018; 230(2): 665–700. doi: 10.1007/s00205-018-1255-z

25. Amstutz S. Sensitivity analysis with respect to a local perturbation of the material property. *Asymptotic Analysis* 2006; 49: 87-108.

26. Amstutz S. Analysis of a level set method for topology optimization. *Optimization Methods and Software* 2011; 26(4-5): 555-573. doi: 10.1080/10556788.2010.521557

27. Bonnet M, Cornaggia R, Guzina B. Microstructural Topological Sensitivities of the Second-Order Macroscopic Model for Waves in Periodic Media. *SIAM Journal on Applied Mathematics* 2018; 78(4): 2057-2082. doi: 10.1137/17M1149018

28. Moulinec H, Suquet P. A numerical method for computing the overall response of nonlinear composites with complex microstructure. *Computer Methods in Applied Mechanics and Engineering* 1998; 157(1): 69 - 94. doi: https://doi.org/10.1016/S0045-7825(97)00218-1

29. Tran TH, Monchiet V, Bonnet G. A micromechanics-based approach for the derivation of constitutive elastic coefficients of strain-gradient media. *International Journal of Solids and Structures* 2012; 49(5): 783 - 792. doi: https://doi.org/10.1016/j.ijsolstr.2011.11.017

30. Dietrich F, Merkert D, Simeon B. Derivation of Higher-Order Terms in FFT-Based Numerical Homogenization. In: Radu FA, Kumar K, Berre I, Nordbotten JM, Pop IS., eds. *Numerical Mathematics and Advanced Applications ENUMATH 2017*Springer International Publishing; 2019; Cham: 289–297.

31. Joyce D, Parnell WJ, Assier RC, Abrahams ID. An integral equation method for the homogenization of unidirectional fibre-reinforced media; antiplane elasticity and other potential problems. *Proceedings of the Royal Society of London A: Mathematical, Physical and Engineering Sciences* 2017; 473(2201). doi: 10.1098/rspa.2017.0080

32. Enrique Sanchez-Palencia AZ. *Homogenization Techniques for Composite Media*. LNP0272Springer. 1 ed. 1987.

33. Andrianov IV, Bolshakov VI, Danishevs'kyy VV, Weichert D. Higher order asymptotic homogenization and wave propagation in periodic composite materials. *Proceedings of the Royal Society of London A: Mathematical, Physical and Engineering Sciences* 2008; 464(2093): 1181–1201. doi: 10.1098/rspa.2007.0267

34. Gambin B, Kröner E. Higher-Order Terms in the Homogenized Stress-Strain Relation of Periodic Elastic Media. *physica status solidi (b)* 1989; 151(2): 513–519. doi: 10.1002/pssb.2221510211

35. Meng S, Guzina BB. On the dynamic homogenization of periodic media: Willis' approach versus two-scale paradigm. *Proceedings of the Royal Society A: Mathematical, Physical and Engineering Science* 2018; 474(2213): 20170638. doi: 10.1098/rspa.2017.0638

36. Sokolowski J, Zochowski A. On the Topological Derivative in Shape Optimization. *SIAM Journal on Control and Optimization* 1999; 37(4): 1251-1272. doi: 10.1137/S0363012997323230

37. Ammari H, Kang H. *Polarization and moment tensors: with applications to inverse problems and effective medium theory*. 162. Springer . 2007.

38. Moulinec H, Suquet P, Milton GW. Convergence of iterative methods based on Neumann series for composite materials: Theory and practice. *International Journal for Numerical Methods in Engineering* 2018; 114(10): 1103-1130. doi: 10.1002/nme.5777

39. Michel JC, Moulinec H, Suquet P. A computational scheme for linear and non-linear composites with arbitrary phase contrast. *International Journal for Numerical Methods in Engineering* 2001; 52(1-2): 139-160. doi: 10.1002/nme.275

40. Monchiet V, Bonnet G. A polarization-based FFT iterative scheme for computing the effective properties of elastic composites with arbitrary contrast. *International Journal for Numerical Methods in Engineering* 2012; 89(11): 1419–1436. doi: 10.1002/nme.3295

41. Allaire G, Gournay dF, Jouve F, Toader AM. Structural optimization using topological and shape sensitivity via a level set method. *Control and Cybernetics* 2005; 34(1): 59-80.

42. Amstutz S, Andrä H. A new algorithm for topology optimization using a level-set method. *Journal of Computational Physics* 2006; 216(2): 573 - 588. doi: https://doi.org/10.1016/j.jcp.2005.12.015

43. Giusti S, Ferrer A, Oliver J. Topological sensitivity analysis in heterogeneous anisotropic elasticity problem. Theoretical and computational aspects. *Computer Methods in Applied Mechanics and Engineering* 2016; 311: 134 - 150. doi: https://doi.org/10.1016/j.cma.2016.08.004

44. Hecht F. New development in FreeFem++. *J. Numer. Math.* 2012; 20(3-4): 251–265.

45. Marigo JJ, Maurel A, Pham K, Sbitti A. Effective Dynamic Properties of a Row of Elastic Inclusions: The Case of Scalar Shear Waves. *Journal of Elasticity* 2017; 128(2): 265–289. doi: 10.1007/s10659-017-9627-4

46. Boutin C, Auriault J. Rayleigh scattering in elastic composite materials. *International Journal of Engineering Science* 1993; 31(12): 1669–1689. doi: 10.1016/0020-7225(93)90082-6

47. Pham K, Maurel A, Marigo JJ. Two scale homogenization of a row of locally resonant inclusions - the case of anti-plane shear waves. *Journal of the Mechanics and Physics of Solids* 2017; 106: 80 - 94. doi: https://doi.org/10.1016/j.jmps.2017.05.001

48. Gangl P. A multi-material topology optimization algorithm based on the topological derivative. 2019. arXiv preprint.

49. Bellis C, Suquet P. Geometric Variational Principles for Computational Homogenization. *Journal of Elasticity* 2018. doi: 10.1007/s10659-018-09713-9